FITTING ERROR ANALYSIS FOR THE VLT DEFORMABLE SECONDARY MIRROR

A. Riccardi[1], M. Xompero[1], L. Busoni[1]
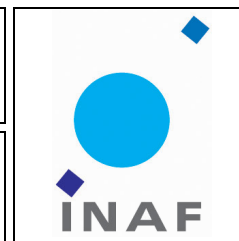
[1]INAF-Osservatorio Astrofisico di Arcetri

Fitting error analysis for the VLT Deformable Secondary Mirror

Armando Riccardi, Marco Xompero, Lorenzo Busoni
INAF-Osservatorio Astrofisico di Arcetri

Prepared by:

(A. Riccardi)

ABSTRACT

The present document reports the results of fitting error analysis for the Deformable Secondary Mirrors (DSM) of the Very Large Telescope (VLT). The analysis is performed in terms of residual rms wave-front error, PSF profile, requested actuator position and force stroke. A comparison with an ideal Karhunen-Loève and Zernike wave-front correctors is also shown. The analysis is based on influence functions simulated by FEA and provided by ADS International Srl. This work has been produced in the framework of OPTICON-JRA1 project (WP 3.5), EU contract RII3-CT-2004-001566.

Doc.No : 002.2005
Version : 3
Date : 18 Jul 2005

ARCETRI-ADOPT
TECHNICAL REPORT

3/36

Modification Record

Version	Date	Author	Section/Paragraph affected	Reason/Remarks
1	17 May 2005	A. Riccardi, M. Xompero	All	First release of the document
1a	18 May 2005	A. Riccardi	4.1, 6.1	
2	17 Jun 2005	A. Riccardi	All (two new sections: 6 and 8)	Post milestone 2 release
3	18 Jul 2005	A. Riccardi	All. New sections: 4, 8, 9, 10.3, 11 and 13	CRD release

Abbreviations, acronyms and symbols

Symbol	Description
AO	Adaptive Optics
OAA	Osservatorio Astrofisico di Arcetri
DSM	Deformable Secondary Mirror
FEA	Finite Element Analysis
INAF	Istituto Nazionale di Astrofisica
KL	Karhunen-Loève
LBT	Large Binocular Telescope
PtV	Peak-to-valley
rms	root mean square
VLT	Very Large Telescope
WF	Wave-front

Symbol	Description
M_{FEA}	Number of FEA mesh point over the thin shell (203904)
M	Number of interpolated points inside the pupil (51084)
N	Number of actuators (1170)
z	Displacement vector over the nodes of the thin shell mesh (M elements) [m]
$\mathbf{z}^{(j)}$	Displacement vector of the *j-th* influence function (M elements) [m]
f	Actuator force vector (N elements) [N]
$\mathbf{f}^{(j)}$	Actuator force vector of the *j-th* influence function (N elements) [N]
p	Vector of actuator displacements (N elements) [m]
$\mathbf{p}^{(j)}$	Vector of actuator displacements of the j-th influence function (N el.) [m]
Z	Influence matrix (MxN) [m/m]
K	Stiffness matrix (NxN) [N/m]
V	Matrix of mirror modes (NxN) [-]
m	Vector of coefficients of mirror modes (N elements) [m]

Contents

1 FEA of shell influence functions

ADS provided the FEA of influence functions for the thin shell deformed by N=1170 electromagnetic actuators. Main parameters are reported in Table 1 and Table 2. The mirror has been simulated using ANSYS with a mesh of M_{FEA}=203904 nodes. The model includes also the effect of the central membrane and the correct interfaces between magnets and shell.

ADS provided to INAF-OAA N=1170 influence functions as M_{FEA}-elements column vectors $\mathbf{z}^{(j)}$ (j=1,…,N) and the corresponding N patterns of actuator forces as N-elements column vectors $\mathbf{f}^{(j)}$ (j=1,…,N). Let's define the "actuator displacement" vector $\mathbf{p}^{(j)}$ as the N-element vector collecting the displacements of the mirror points corresponding to the center of

ITEM	Value
Density	2530 Kg/m^3
Young modulus	90.6 GPa
Poisson	0.25
Central hole diameter	96 mm
External diameter	1120 mm
Radius of curvature	4553.57 mm
Thickness	2 mm

Table 1. Parameters used for the shell FEA

the actuators for the influence function $\mathbf{z}^{(j)}$. In the framework of the present FEA, the *j-th* influence function $\mathbf{z}^{(j)}$ has been obtained constraining (*i* is an index running on the actuator number):

(1) $\begin{cases} p_i^{(j)} = 1 \mu m & \text{if} \quad i = j \\ p_i^{(j)} = 0 \mu m & \text{if} \quad i \neq j \end{cases}$.

That corresponds to simulate influence functions with actuator coupling equal to zero.

2 FEA data preprocessing and used reconstruction algorithms

FEA data $\mathbf{z}^{(j)}$ have been interpolated over a 256x256 (M=51084 inside the pupil) regular grid in

Ring	Ring angle (deg)	# of act.s per ring	Total # of act.s
1	63.26	14	14
2	91.81	20	34
3	120.32	26	60
4	148.83	32	92
5	177.33	38	130
6	205.83	44	174
7	234.32	50	224
8	262.80	56	280
9	291.27	62	342
10	319.73	68	410
11	348.17	74	484
12	376.60	80	564
13	405.02	86	650
14	433.42	92	742
15	461.80	98	840
16	490.17	104	944
17	518.52	110	1054
18	546.84	116	1170

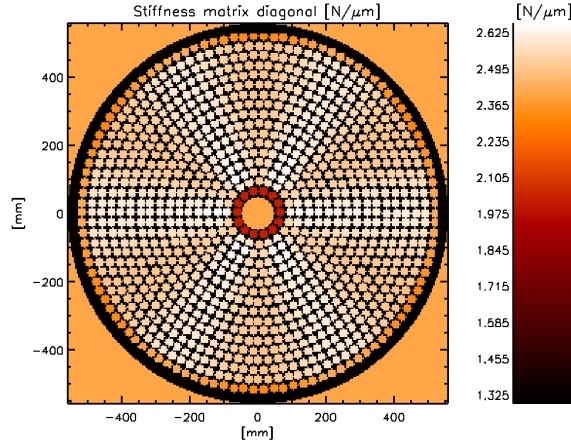Table 2. Actuator geometry. See Ref. [1] for more details.

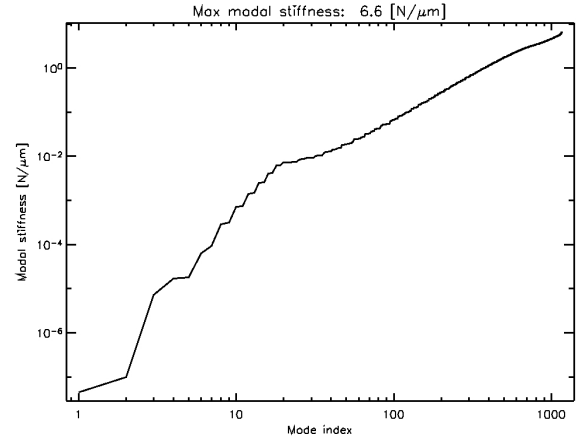Fig. 1. Local stiffness: diagonal of stiffness matrix.

Fig. 2. Modal stiffness. Modes ordered from least to most stiff.

order to reduce the size of the matrices to use and match the regular grid of the simulated wave-fronts (see Sec. 5). The pixel pitch is 4.38 mm over the thin shell (31.8 mm over the primary) corresponding to 6.60 pixels per actuator pitch=28.9 mm (average value). The adimensional MxN $\mathbf{Z}$ matrix, collecting all the $\mathbf{z}^{(j)}/1\mu m$ as columns, represents the influence matrix. A generic deformation $\mathbf{z}$ is related to the corresponding actuator displacement vector $\mathbf{p}$ by the simple equation

(2) $\quad \mathbf{z} = \mathbf{Zp}$.

We used the standard least-square fitting formula to fit a generic wave-front $\mathbf{w}$ (M-element vector):

(3) $\quad \mathbf{p} = \left(\mathbf{Z}^T \mathbf{Z} \right)^{-1} \mathbf{Z}^T \mathbf{w} / 2$,

where the factor ½ is considered to account for the mirror reflection. The reconstructed wave-front $\mathbf{w}_r$ and the corresponding error $\boldsymbol{\varepsilon}$ are computed as

(4) $\quad \mathbf{w}_r = 2\mathbf{Zp} = \mathbf{Z}(\mathbf{Z}^T\mathbf{Z})^{-1}\mathbf{Z}^T\mathbf{w}$,

(5) $\quad \boldsymbol{\varepsilon} = \mathbf{w} - \mathbf{w}_r = \left[\mathbf{I} - \mathbf{Z}(\mathbf{Z}^T\mathbf{Z})^{-1}\mathbf{Z}^T \right]\mathbf{w}$.

Finally the fitting error is computed as

(6) $\quad \sigma_{\text{fit}}^2 = \left\langle \boldsymbol{\varepsilon}^T \boldsymbol{\varepsilon} \right\rangle - \left\langle \boldsymbol{\varepsilon} \right\rangle^T \left\langle \boldsymbol{\varepsilon} \right\rangle$,

where the symbol $\langle \cdots \rangle$ represents the ensemble average obtained, in the present simulation, averaging the results of 10 thousands uncorrelated wave-fronts (see Sec. 5).

The NxN $\mathbf{K}$ matrix, collecting all the $\mathbf{f}^{(j)}/1\mu m$ as columns, represents the stiffness matrix. A generic pattern of forces $\mathbf{f}$ is related to the corresponding actuator displacement vector $\mathbf{p}$ by the simple equation

(7) $\quad \mathbf{f} = \mathbf{Kp}$

The diagonal of the stiffness matrix is shown in Fig. 1. It represents the local stiffness to move just a single actuator keeping the others in their zero location. The singular value decomposition (SVD) of matrix K

(8) $\quad \mathbf{K} = \mathbf{USV}^T$, $\mathbf{S} = \text{diag}(s_1, \cdots, s_{1170})$, $\mathbf{V}$ and $\mathbf{U}$ orthogonal,

defines, through the $\mathbf{V}$ matrix, the base of stiffness modes. The modal coefficient vector $\mathbf{m}$ is defined by the relationship
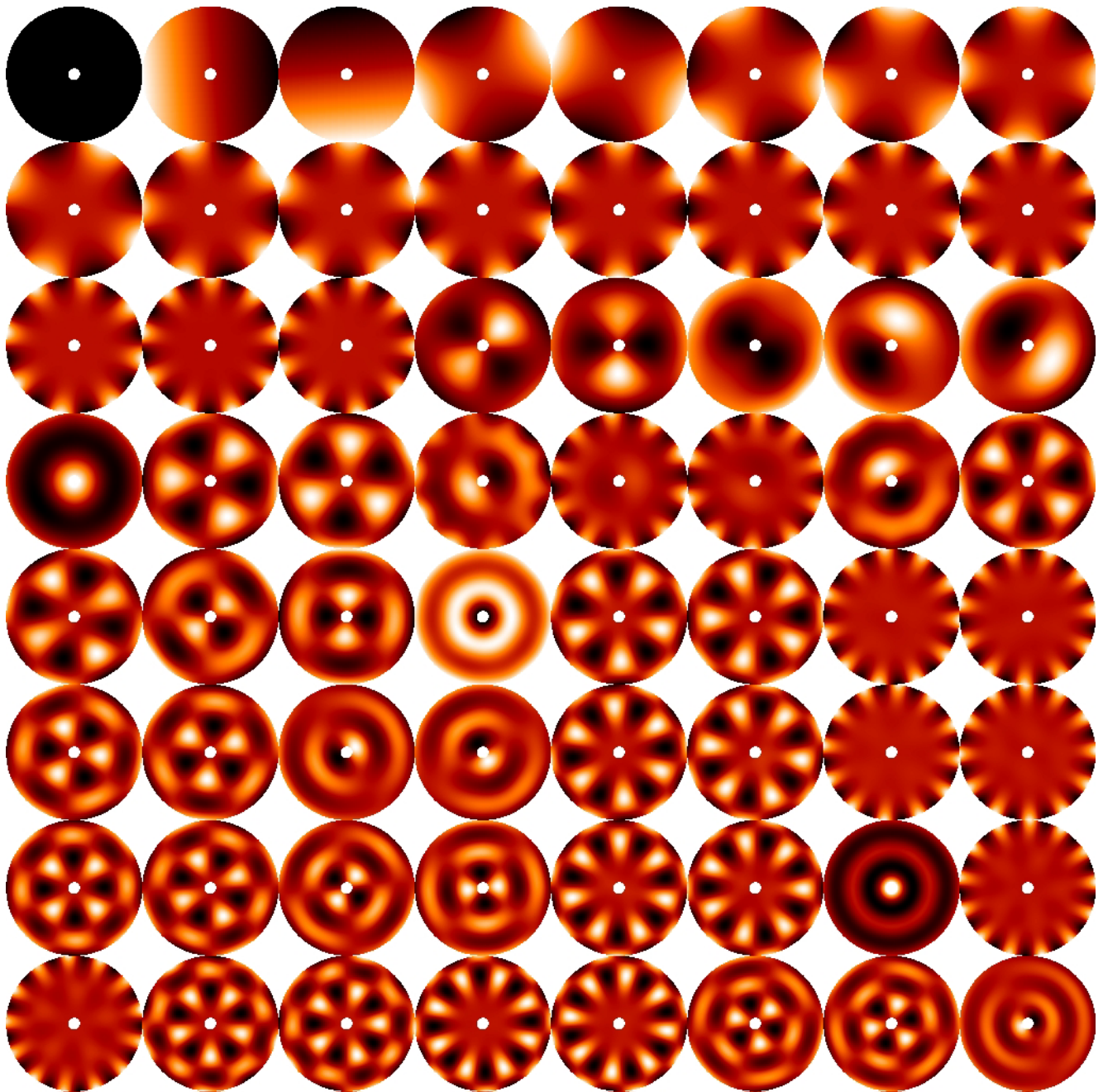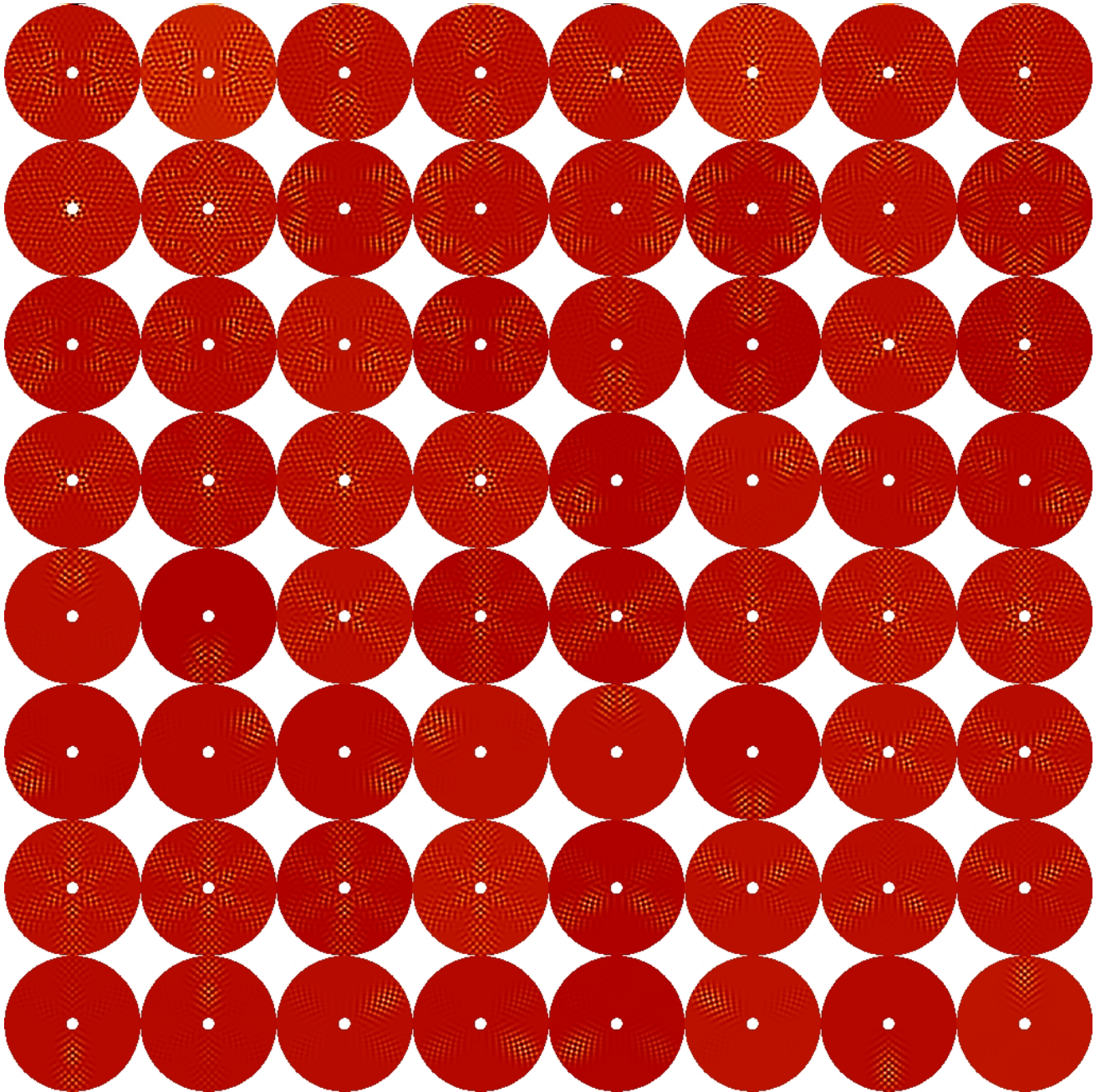
Fig. 3. First 64 least stiff mirror modes.

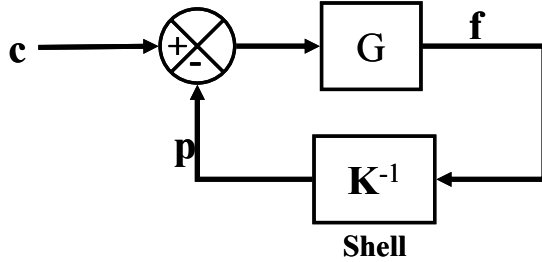Fig. 4. Last 64 most stiff mirror modes.

Fig. 5. Scheme of internal control loop of actuator positions. For fitting error purposes only quasi-static terms have been considered.
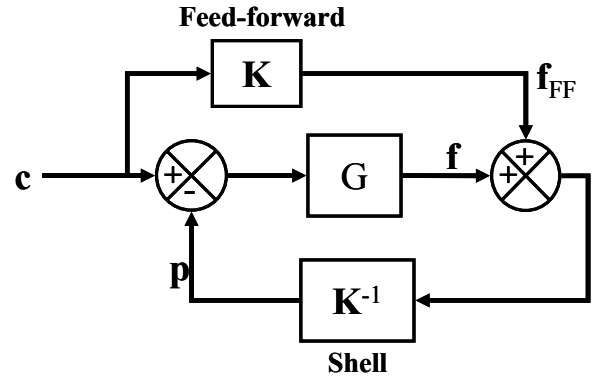
Fig. 6. Scheme of internal control loop of actuator positions using feed-forward force.

(9) $\mathbf{m} = \mathbf{V}^T \mathbf{p}$, or $\mathbf{p} = \mathbf{V}\mathbf{m}$.

Fig. 2 shows the diagonal of matrix $\mathbf{S}$, that represents the stiffness of the modes. Fig. 3 shows the least stiff (piston-like, tip-tilt-like, astigmatism-like, etc.) and Fig. 4 the stiffest modes. The mirror shape of the modes is computed, using Eqs. (2) and (9), as

(10) $\mathbf{z} = \mathbf{Z}\mathbf{V}\mathbf{m}$

Combining Eq. (2) and (9), we computed the modal least-square fitting as:

(11) $\mathbf{m} = \mathbf{V}^T \left(\mathbf{Z}^T \mathbf{Z} \right)^{-1} \mathbf{Z}^T \mathbf{w} / 2$

3   Actuator coupling and fitting error

For a defined interface between actuators (i.e. magnets in our case) and thin shell, the actuator coupling depends on the ratio between the stiffness of the shell and the stiffness of the actuators. That can be tuned changing the shell thickness and, for electromagnetic actuators, the gain of the internal control loop using the capacitive sensor feed-back.

Referring to Fig. 5, the relation between the position command vector $\mathbf{c}$ and the actuator position vector $\mathbf{p}$ is given by

(12) $\mathbf{p} = \left(\mathbf{I} + \dfrac{\mathbf{K}}{G} \right)^{-1} \mathbf{c}$,

where $\mathbf{K}$ is the stiffness matrix of the glass shell and G is the 0Hz gain of the internal control loop. Eq. (12) is also valid in the case of piezo-stack mirrors where $\mathbf{c}$ represents the voltage command and G is the axial stiffness of the piezo rods. The zero-coupling case ($\mathbf{c} = \mathbf{p}$) is obtained with $G \gg |\mathbf{K}|$ or considering the feed-forward configuration of Fig. 6. The feed-forward configuration is currently the one implemented in the DSM internal control. Fig. 7 shows an example of normalized influence functions with different values of G.
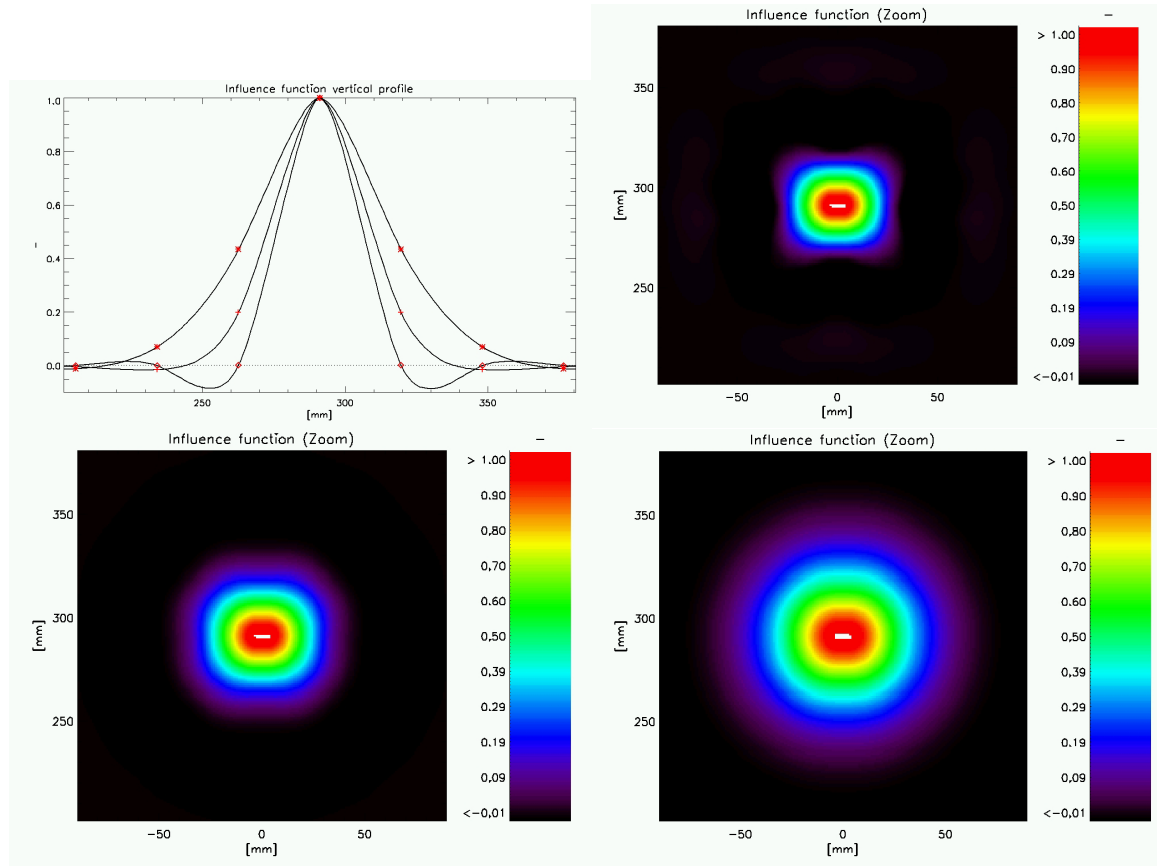
Fig. 7. Example of normalized (unit peak) influence functions (actuator of the ring nine at x=0) with different static G gain values. Top-right: infinity (feed-forward, 0% actuator coupling); bottom-left: 2.5 N/μm (20% actuator coupling); bottom-right: 0.4N/μm (usual gain value, 45% act coupling).

Let's define $\mathbf{Q}_G = \mathbf{I} + \mathbf{K}/G$. Note that $\mathbf{Q}_G$ is not-singular because it is the sum between an identity matrix and a stiffness matrix (i.e. eigenvalues ≥ 0). Considering Eqs. (2) and (12), the relationship between a generic shell deformation $\mathbf{z}$ and the command vector $\mathbf{c}$ is given by

(13) $\mathbf{z} = \mathbf{Z}\mathbf{Q}_G^{-1}\mathbf{c}$.

The least-square fitting of a generic wave-front $\mathbf{w}$ can be obtained as

(14) $\mathbf{c} = \left[\left(\mathbf{Z}\mathbf{Q}_G^{-1}\right)^T \mathbf{Z}\mathbf{Q}_G^{-1}\right]^{-1}\left(\mathbf{Z}\mathbf{Q}_G^{-1}\right)^T \mathbf{w}/2 = \mathbf{Q}_G\left(\mathbf{Z}^T\mathbf{Z}\right)^{-1}\mathbf{Z}^T\mathbf{w}/2$.

Finally, combining the last two equations, the reconstructed wave-front $\mathbf{w}_{rG}$ is

(15) $\mathbf{w}_{rG} = \left(\mathbf{Z}\mathbf{Q}_G^{-1}\right)\left[\mathbf{Q}_G\left(\mathbf{Z}^T\mathbf{Z}\right)^{-1}\mathbf{Z}^T\mathbf{w}/2\right] = \mathbf{Z}\left(\mathbf{Z}^T\mathbf{Z}\right)^{-1}\mathbf{Z}^T\mathbf{w} = \mathbf{w}_r$.

$\mathbf{w}_{rG}$ results to be <u>exactly</u> equal to $\mathbf{w}_r$, the result obtained with zero-coupling influence functions stated in Eq. (4). It demonstrates that fitting error is <u>not</u> depending on the actuator coupling (changeable with G). The actuator coupling is a wrong parameter to specify the ability of the system to correct turbulence in terms of fitting error. The fitting error can only be modified changing the actuator-to-mirror interface, the actuator geometry and the edge constrains of the shell. The last item does not apply to DSMs because the outer edge is always free (at least for under-sized secondary mirrors).
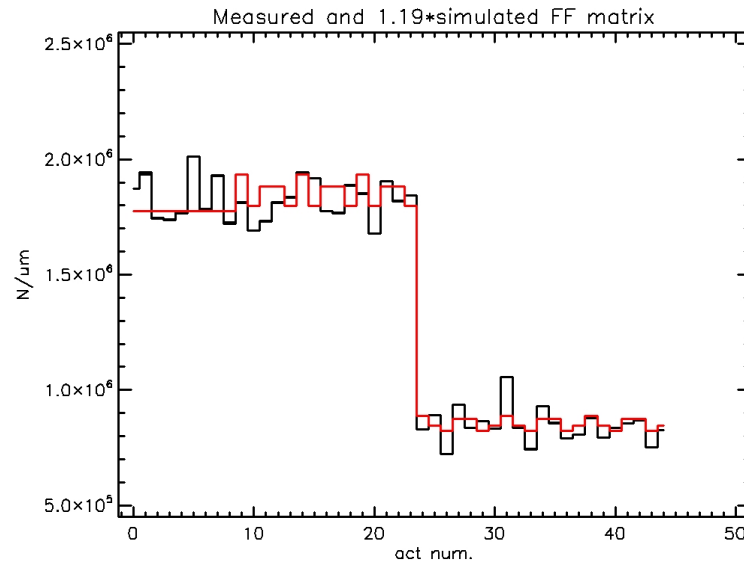
Fig. 8 Preliminary comparison between diagonal of measured P45 feed-forward matrix (black) and FEA simulated data (red). FEA data are rescaled of a factor 1.19. Actuators are not perfectly calibrated yet.

Because of the previous result, the current analysis is performed using the zero-coupling influence functions ($\mathbf{c} = \mathbf{p}$).

4   Preliminary validation of FEA simulations

In order to validate the FEA models for the influence function computation and the code to produce results presented in this paper, we compared measured data obtained on the LBT adaptive secondary prototype P45 (45 actuator, 3 rings and diameter 240 mm) with FEA simulations of the same unit. In particular we compared the FEA feed-forward matrix (stiffness matrix in terms of displacement over capacitive sensor armatures) with the corresponding measurements on P45. The stiffness of the FEA matrix is underestimated of 19% (see Fig. 8). The result has to be considered as preliminary, because the P45 actuators are not yet well calibrated because of schedule problems. The subject is currently under investigation. In case 19% excess of stiffness would be confirmed, the numerical results of the present work are still valid considering a shell of thickness 1.88 mm instead of 2.0 mm.

5   Simulated wave-fronts

In order to compute the statistical average of the relevant parameters, we generated 10 thousands wave-fronts using CAOS simulation package [4]. Simulation parameters are reported in Table 3. Because of the finite sampling over the pupil, the FFT algorithm used to generate the wave-fronts does not simulate turbulence at spatial frequencies $\mathbf{k}$ larger then $2\pi/(2l_p)$ ($|k_x| > \pi/l_p$, $|k_y| > \pi/l_p$). This contribution can be estimated in terms of its rms σ_{NS} and is added as uncorrelated error to the fitting residuals obtained by the numerical simulations. The variance σ_{NS}^2 is given by

Parameter	Value
Number of wave-fronts	10000
Spectrum type	Kolmogorov
Used algorithm	FFT + sub-harmonics adding
FFT grid	256x256
Number of sub-harmonics orders	10
Pupil sampling	256x256
Sample points per actuator pitch	6.60
Shell diameter (D)	1120 mm
Primary optical diameter (D_p)	8115 mm
Sampling over the shell (l_s)	4.38 mm
Projected sampling on the primary (l_p)	3.17 cm
Median seeing@30deg: r_0(0.5μm)	12.1 cm
Bad seeing: r_0(0.5μm)	5.2 cm
Non simulated wave-front rms:	
Median seeing	12.5 nm rms
Bad seeing	25.2 nm rms

Table 3. Parameters for wave-front generation.

$$(16) \quad \sigma_{NS}^2 = \frac{1}{(2\pi)^2} \iint_{|k_x|,|k_y|>\pi/l_p} \Phi_{OPD}(\mathbf{k})\mathrm{d}\mathbf{k} = 0.229\left(\frac{\lambda}{2\pi}\right)^2\left(\frac{l_p}{r_0}\right)^{5/3} ,$$

where $\Phi_{OPD}(\mathbf{k})$ is the Kolmogorov power spectrum of the turbulence optical path difference (OPD)

$$(17) \quad \Phi_{OPD}(\mathbf{k}) = 19.34\frac{(\lambda/2\pi)^2}{k^{11/3}r_0^{5/3}} .$$

Numerical values of σ_{NS} are reported in Table 3.

Fig. 9 shows the statistical average of residual rms wave-front error removing up to 1170 Zernike and Karhunen-Loève (KL) modes. KL modes have been obtained from Ref. [5] (M. Kasper's code, ESO). The relative behavior between the Zernike and KL curves is in good agreement with the theory [6]. Numerical values are reported in Table 4. The simulation produces conservative results with respect to theory regarding the 1170-Zernike fitting error (4%). The simulation underestimates the Kolmogorov low order modes of about 8% due to the nature of the FFT algorithm that tends to produce a finite outer-scale L_0. The 8% error is compatible to a value of L_0=4.5-6.0 km instead of

Median seeing case	Wave-front residual		error
	Simulated	Theorical	
Piston-removed residual	2.49 μm rms	2.70 μm rms	-8%
1170 Zernike removed	70.0 nm rms	67.4 nm rms	+4%
1170 KL removed	60.2 nm rms		

Table 4. Comparison between simulated and theoretical data. KL theorical value correcting 1170 modes is not reported because no analytical expression is reported in literature.
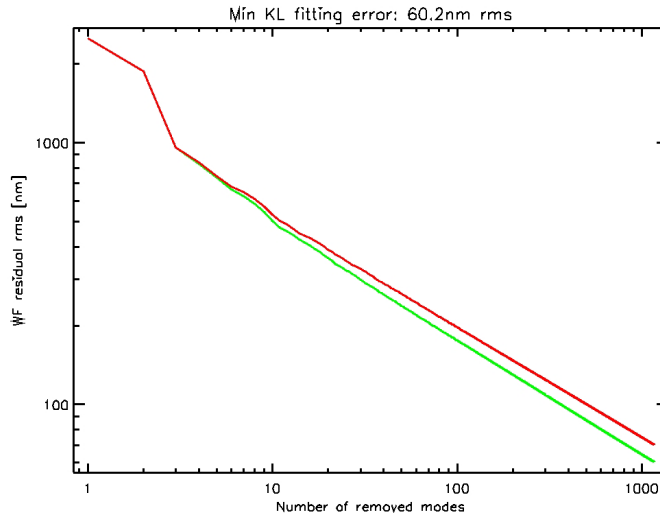
Fig. 9. Median seeing case. Comparison between Zernike (red line) and KL (green line) fitting error as a function of the number of removed modes. The relative difference removing 500 modes is 13.3% in agreement with Dai (Ref. [6], Fig. 1: 13.6%).

infinity [7][8]. Because L_0 is expected to be less then 100m the simulation gives conservative results (with respect to the expected L_0) even in the low-order regime.

6 Numerical simulation results: full correction

In the present section we show the results of the simulation when all the 1170 degrees of freedom are used to fit the turbulence. Results are simulated applying 10000 uncorrelated wave-fronts. The fitting error thresholds are those specified in Ref. [2] (80 nm rms and 150 nm rms for median and bad seeing respectively) reduced by the specified contribution of the static mirror flattening residual (15 nm rms). That gives a fitting error threshold of 78 nm rms and 149 nm rms for median and bad seeing conditions respectively.

6.1 Median seeing case

Results of fitting error correcting all modes in the median seeing case are summarized in Table 6. Fig. 10 and Fig. 11 show the actuator maps of required actuator stroke (PtV) and position rms. Fig. 12 and Fig. 13 show, respectively, the maps of the maximum absolute value and rms of applied force. Fitting error is below the specified threshold and values of rms and peak force are not critical. In particular the peak force is below 1 N, which is the current threshold for LBT actuator driver design.

Fig. 13 shows the distribution of the residual wave-front rms over the pupil. In the last figure is evident that the dominant spatial scale of the residual is the inter-actuator distance. This pattern is typical for any AO corrector with localized actuators and produces peaks around the PSF core at an angular distance λ/l (λ is the wavelength and l is the actuator pitch projected to the primary). The secondary peaks are located on the vertex of a hexagon because the actuator pattern is almost-hexagonal. The effect of not perfect hexagonal pattern produces the local splitting of the secondary

peaks in sub-parts. This effect is clearly shown in the V-band PSF map and profiles in Fig. 15 Fig. 16. The PSF simulation considers only the fitting error effects. No spider or features introduced by other parts of the AO loop are considered. The aim is to determine the unavoidable effects due to the DSM actuator geometry and spacing on the system performances.

Finally Fig. 17 reports the V-band Strehl ratio distribution, giving an estimation of the variability of this parameter due to fitting error.

Fig. 20, Fig. 19 and Fig. 21 show analogous PSF results for the K-band. Contribution of secondary peaks is heavily reduced in this case because of the high obtained Srehl ratio.

6.2 Bad seeing case

The bad seeing data, shown in Fig. 23 to Fig. 27 and Table 7, are a simple scaling of the median seeing case. Values of rms and peak force are critical in this case. The force requirements can be relaxed reducing the number of corrected modes considering that the fitting error is well below the specified threshold (see Sec. 10.2). An alternative solution is to reduce the stiffness of the shell reducing its thickness as shown in Table 5. The latter solution has the drawback of making the manufacturing and handling of the shell more critical.

Shell thickness	mm	2	1.8	1.7	1.6
max peak force	N	1.66	1.21	1.02	0.85
max rms actuator force	N rms	0.35	0.26	0.22	0.18
rms force	N rms	0.32	0.23	0.2	0.16

Table 5 Reduction of forces in <u>bad seeing</u> conditions depending on shell thickness. Peak force goes below 1N threshold with thickness less then 1.7 mm. In this conditions the manufacturing and handling of the shell is critical.
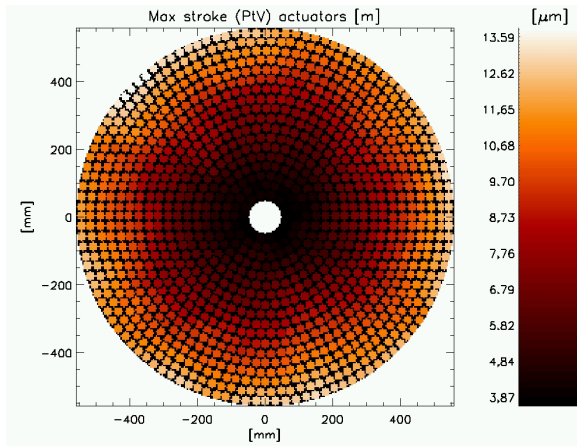
Fig. 10. PtV actuator stroke in median seeing conditions. Result of fitting 10000 uncorrelated wave-fronts.
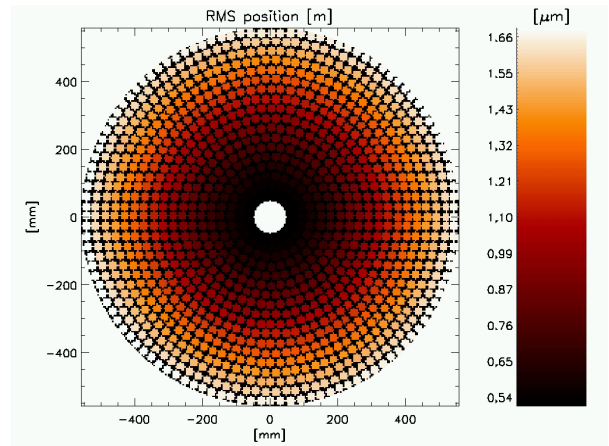

Fig. 11 Actuator position rms in median seeing conditions. Result of 10000 uncorrelated wave-fronts.
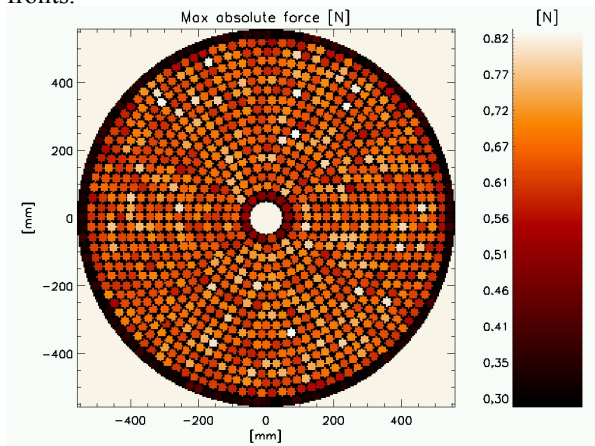

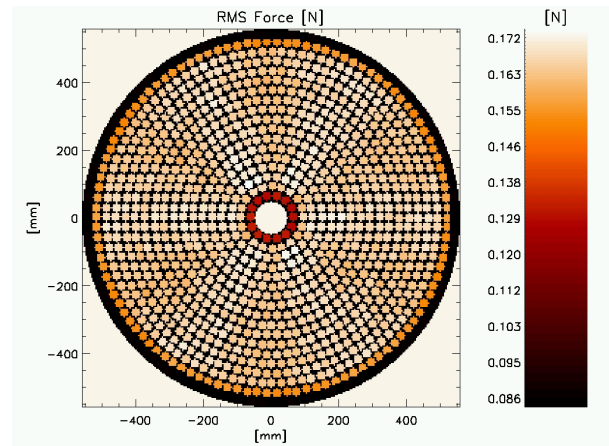Fig. 12. Peak actuator force in median seeing conditions. Result of fitting 10000 uncorrelated wave-fronts.

Fig. 13 Rms actuator force in median seeing conditions. Result of fitting 10000 uncorrelated wave-fronts.
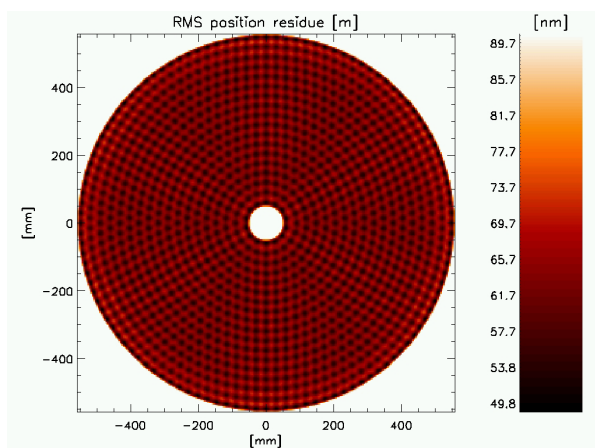

Fig. 14 Pupil map of the rms WF residual in median seeing conditions. Result of fitting 10000 uncorrelated wave-fronts.

Parameter	Value
Median seeing@30deg: r_0(0.5μm)	12.1 cm
Specified fitting error	78 nm rms
Fitting error (all modes)	62.5 nm rms
1170 Zernike modes fitting error	70.0 nm rms
1170 KL modes fitting error	60.2 nm rms
max PtV actuator displacement	13.6 μm
max rms actuator displacement	1.66 μm rms
max peak force	0.82 N
max rms actuator force	0.17 N rms
rms force	0.157 N rms

Table 6. Resume of the simulation results in the median seeing case. Results of fitting 10000 uncorrelated wave-fronts.
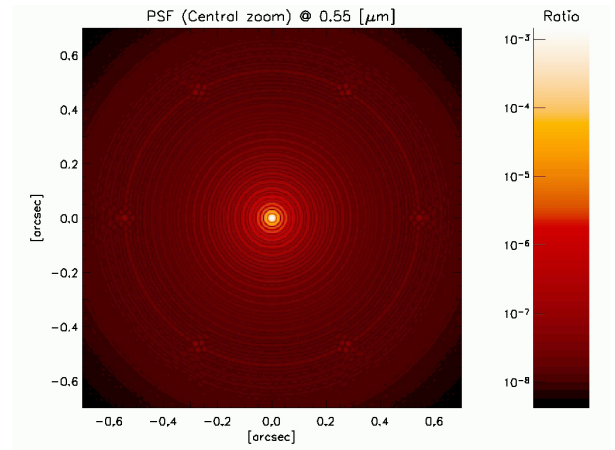
Fig. 15. Median seeing conditions. V-band, 10000 uncorrelated wave-fronts. PSF. Six spots at λ/l=0.54 arcsec are due to the quasi-hexagonal pattern of actuators with average pitch l projected to primary.
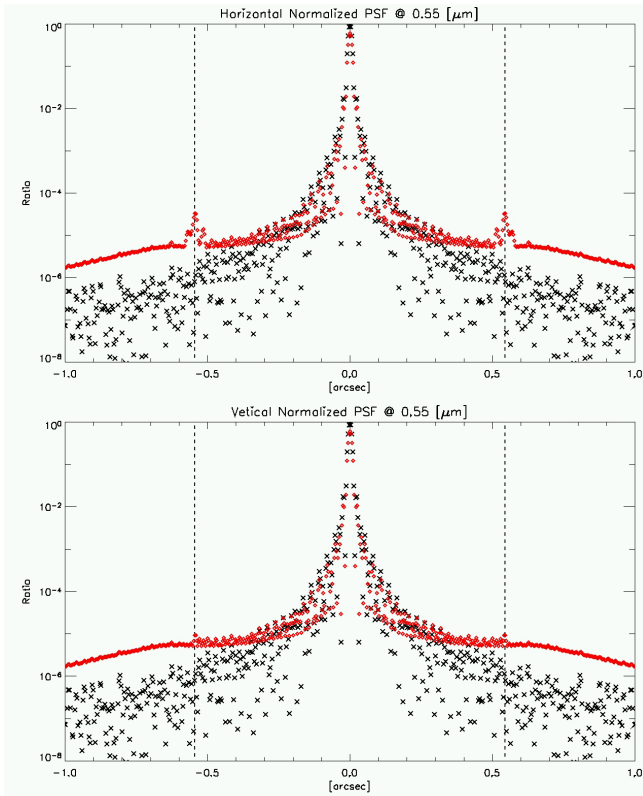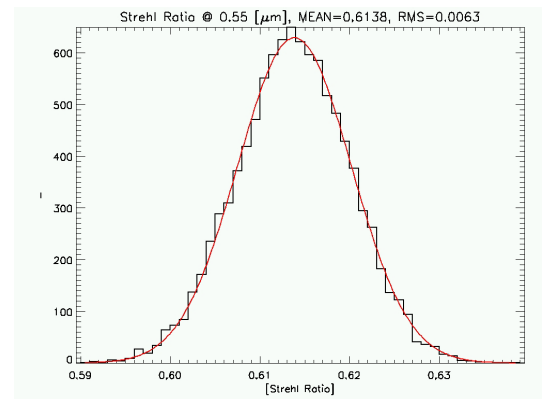

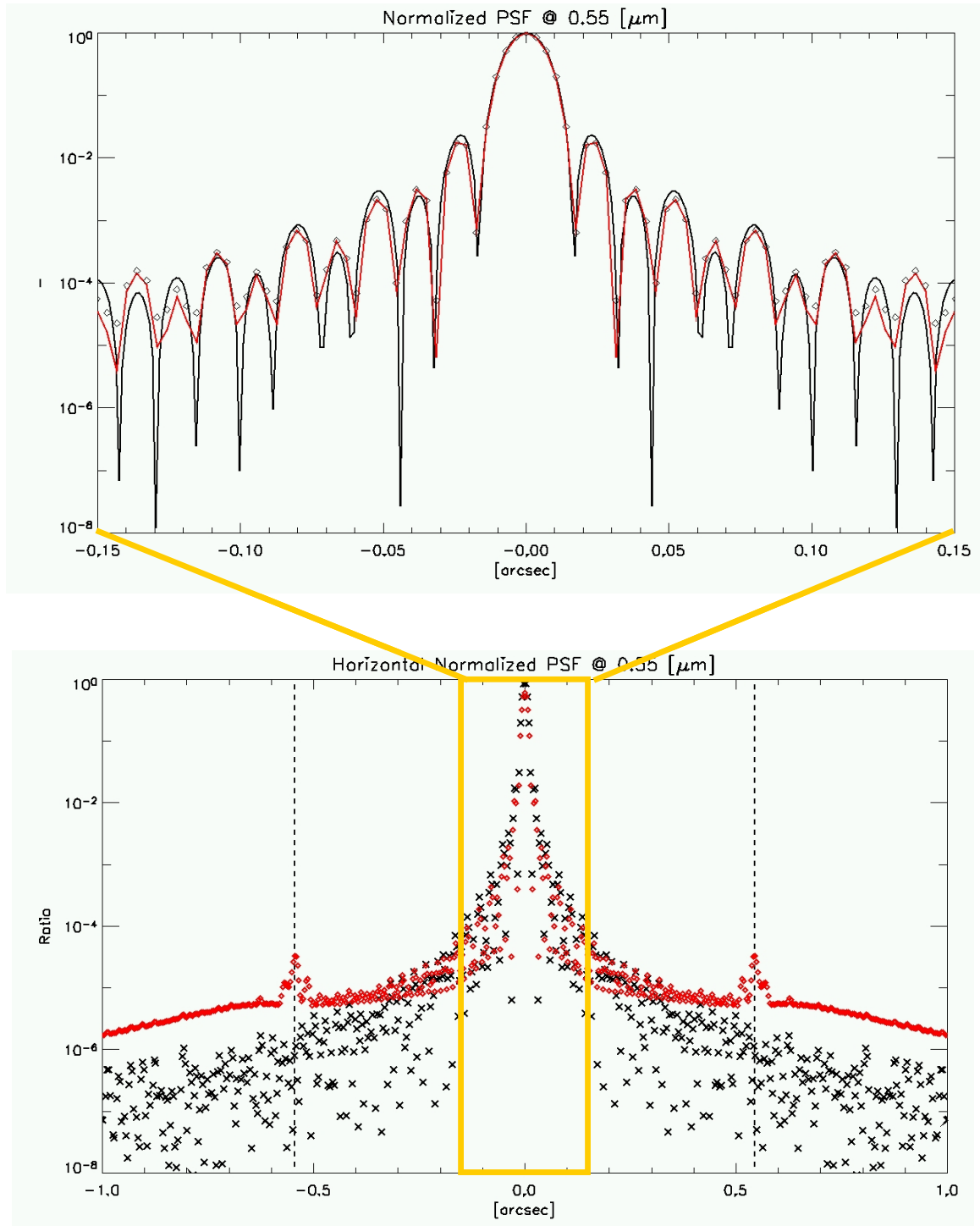Fig. 16. Median seeing conditions. V-band, 10000 uncorrelated wave-fronts. Red diamonds: corrected PSF. Black crosses: diffraction limited PSF. Top: PSF x-cut. Bottom: PSF y-cut. Only fitting error is considered. Vertical dashed lines are located to λ/l=0.54 arcsec. (l average actuator separations projected to primary mirror).

Fig. 17. Median seeing conditions. V-band, 10000 uncorrelated wave-fronts. Histogram of Strehl ratio values.

Fig. 18 Zoom of Fig. 16 to show the diffraction limited rings with more details.
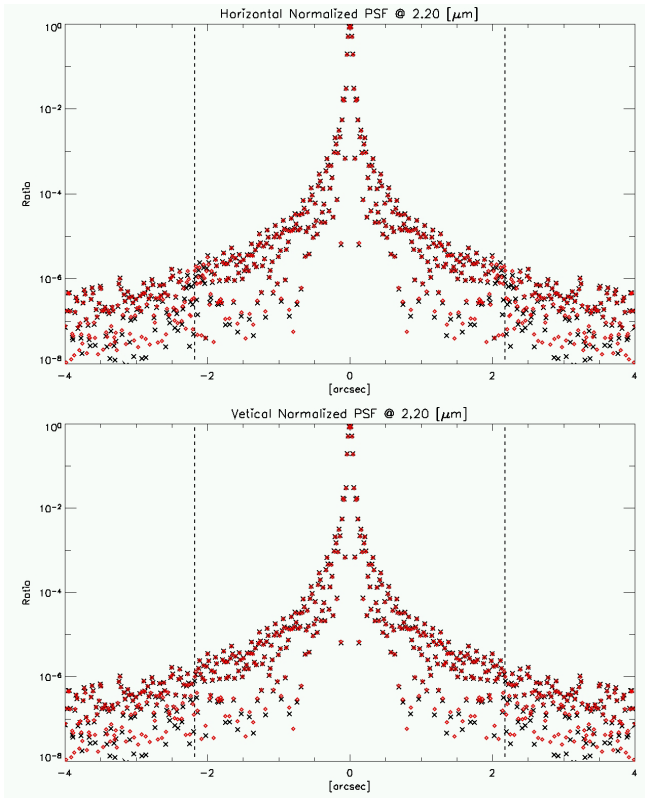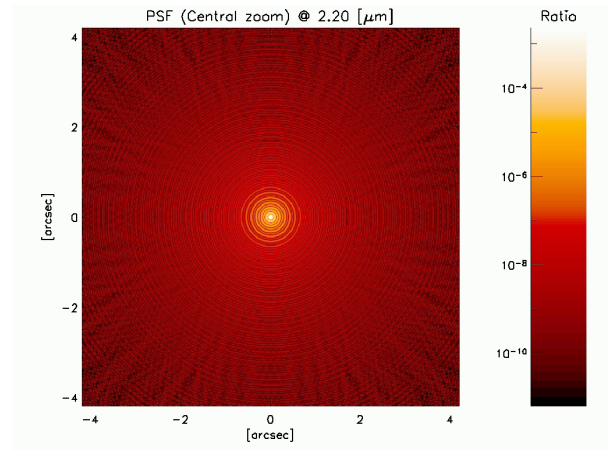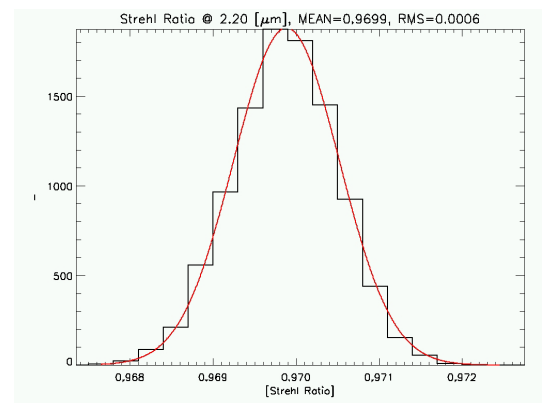
Fig. 20. Median seeing conditions. K-band, 10000 uncorrelated wave-fronts. PSF.

Fig. 19. Median seeing conditions. K-band, 10000 uncorrelated wave-fronts. Red diamonds: corrected PSF. Black crosses: diffraction limited PSF. Top: PSF x-cut. Bottom: PSF y-cut. Only fitting error is considered. Vertical dashed lines are located to λ/l=2.2 arcsec. (l average actuator separations projected to primary mirror).

Fig. 21. Median seeing conditions. K-band, 10000 uncorrelated wave-fronts. Histogram of Strehl ratio values. Only fitting error is considered.
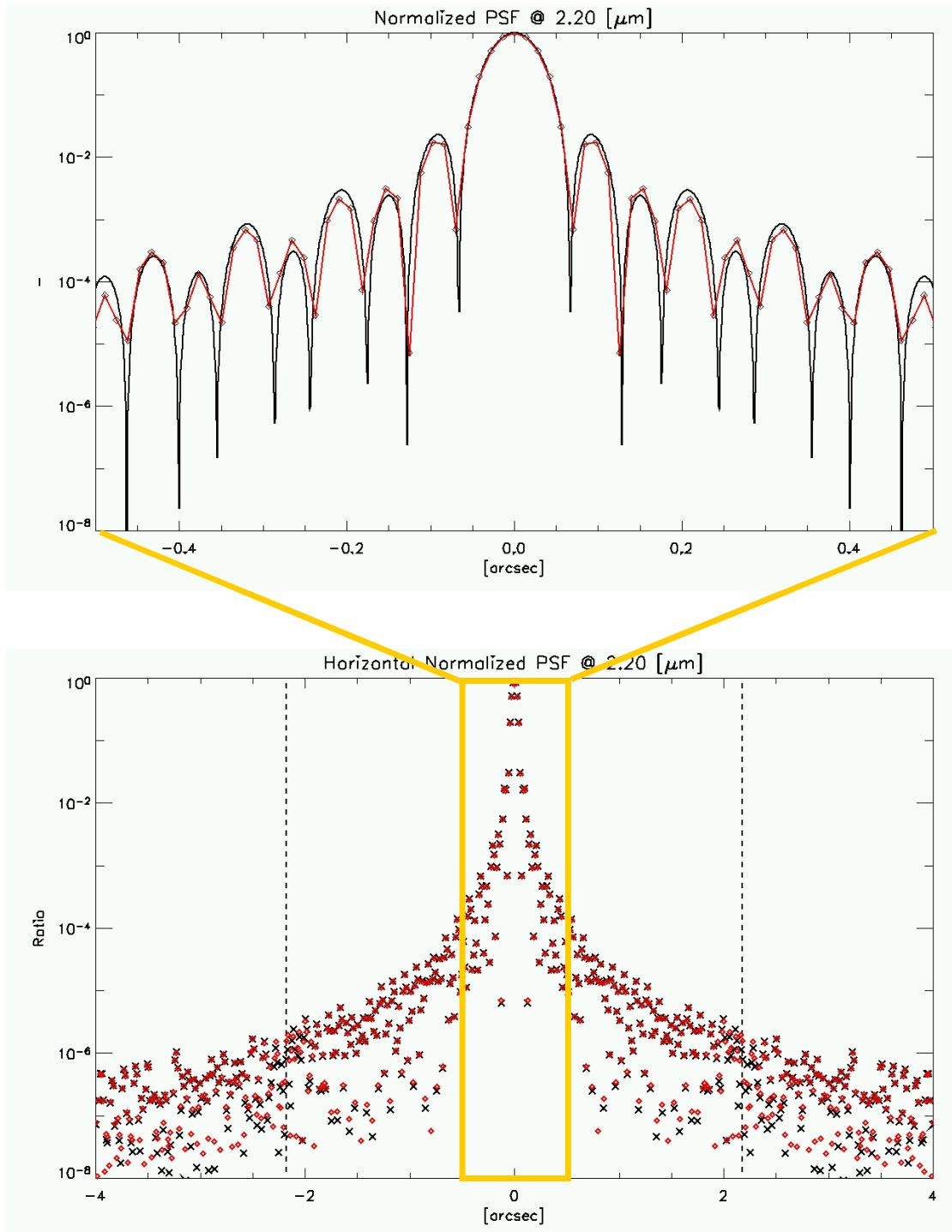
Fig. 22 Zoom of Fig. 19 to show the diffraction limited rings with more details.
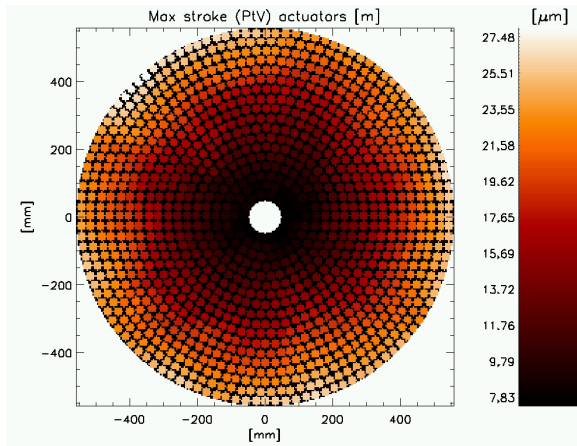
Fig. 23. PtV actuator stroke in bad seeing conditions. Result of fitting 10000 uncorrelated wave-fronts.
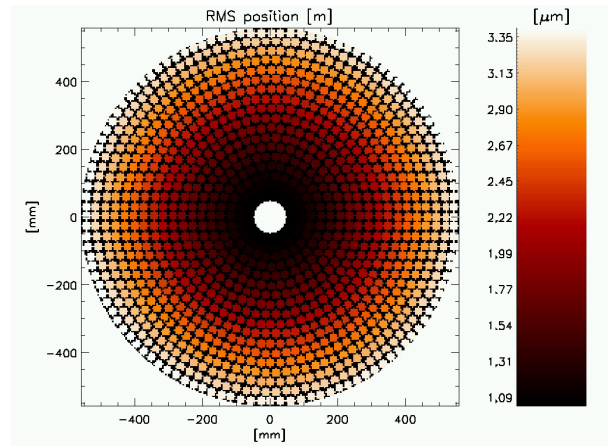

Fig. 24. PtV actuator stroke in bad seeing conditions. Result of fitting 10000 uncorrelated wave-fronts.
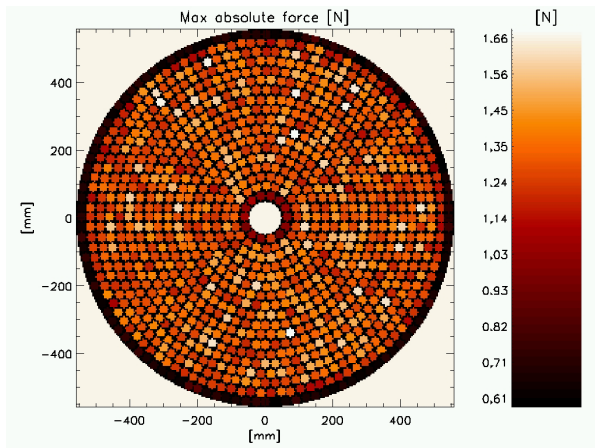

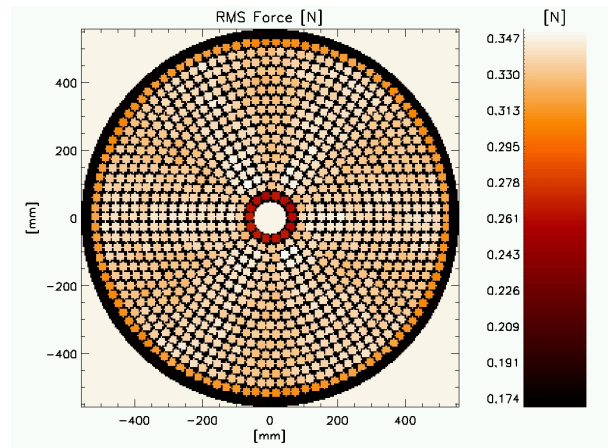Fig. 25. Peak actuator force in bad seeing conditions. Result of fitting 10000 uncorrelated wave-fronts.

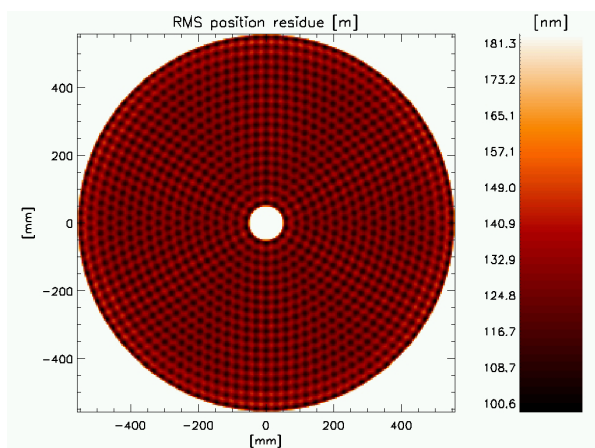Fig. 26 Rms actuator force in bad seeing conditions. Result of fitting 10000 uncorrelated wave-fronts.

Fig. 27 Pupil map of the rms WF residual in bad seeing conditions. Result of fitting 10000 uncorrelated wave-fronts.

Parameter	Value
Bad seeing: $r_0(0.5\mu m)$	5.2 cm
Specified fitting error	149 nm rms
Fitting error (all modes)	126 nm rms
1170 Zernike modes fitting error	141 nm rms
1170 KL modes fitting error	122 nm rms
max PtV actuator displacement	27.5 μm
max rms actuator displacement	3.36 μm rms
max peak force	1.66 N
max rms actuator force	0.35 N rms
rms force	0.317 N rms

Table 7. Resume of the simulation results in the bad seeing case. Results of fitting 10000 uncorrelated wave-fronts.
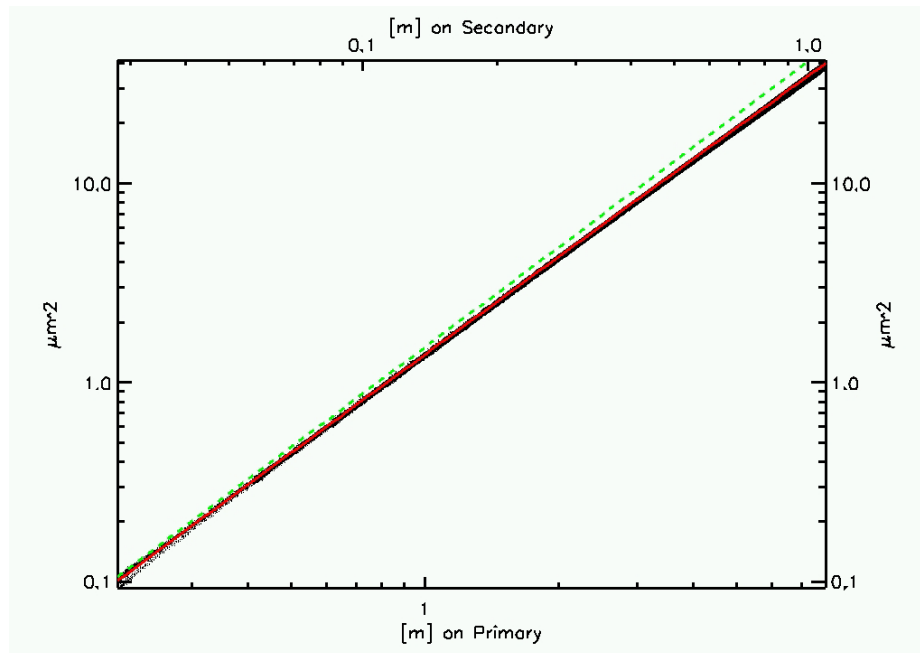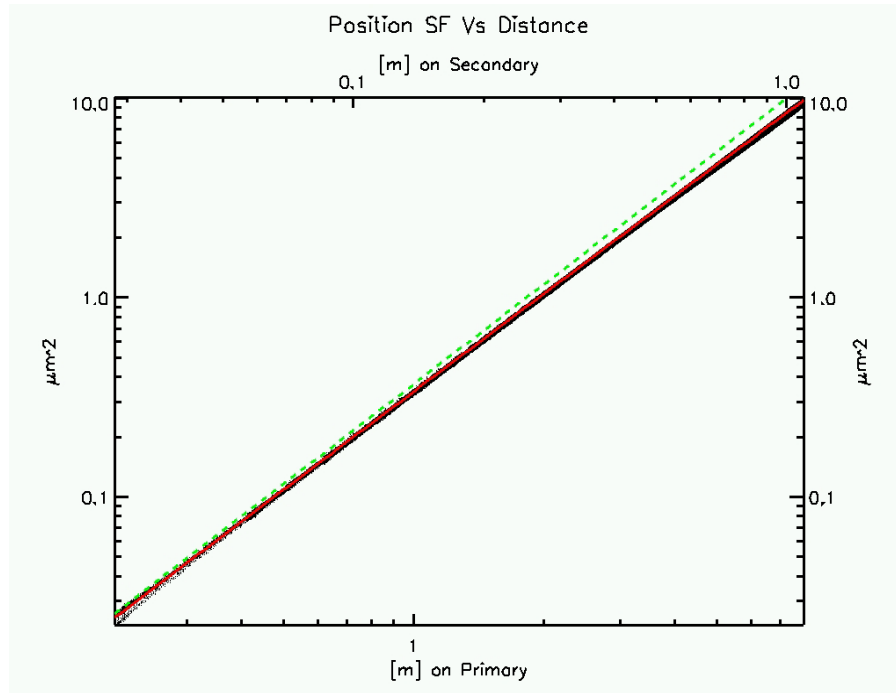
Fig. 28 Actuator position structure function in median (top) and bad (bottom) seeing conditions. Black: actuator position structure function. Green dashed: ¼ kolmogorov structure function. Red solid: ¼ Von Karman structure function with L0=6km.
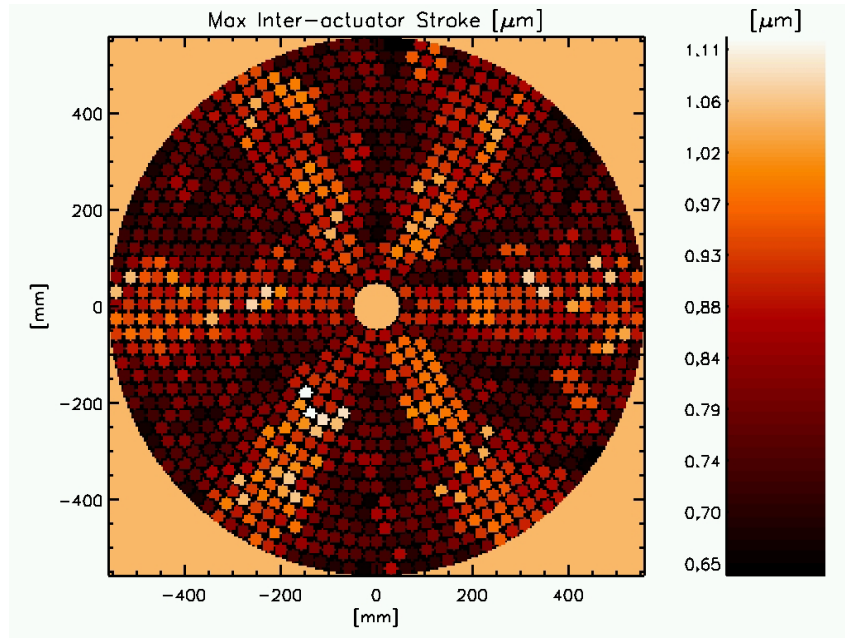
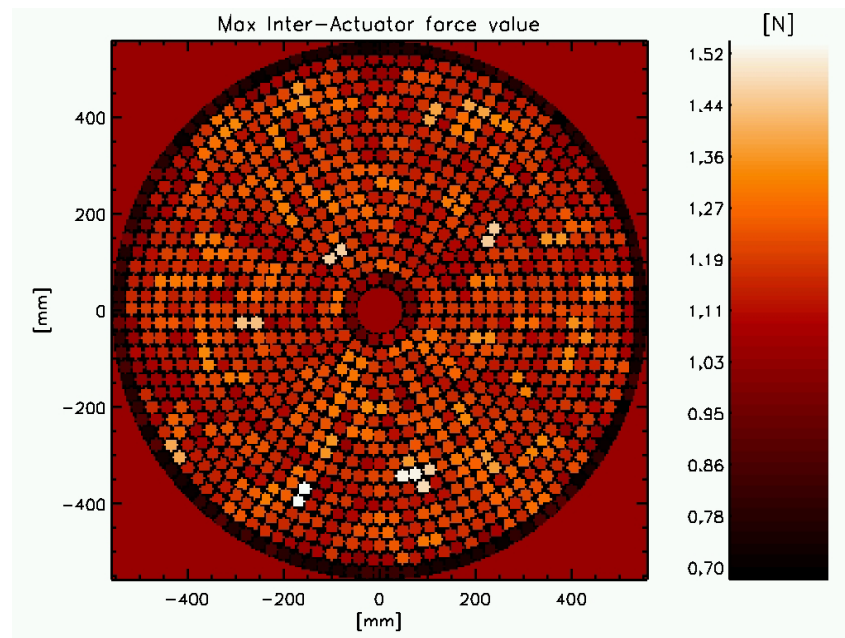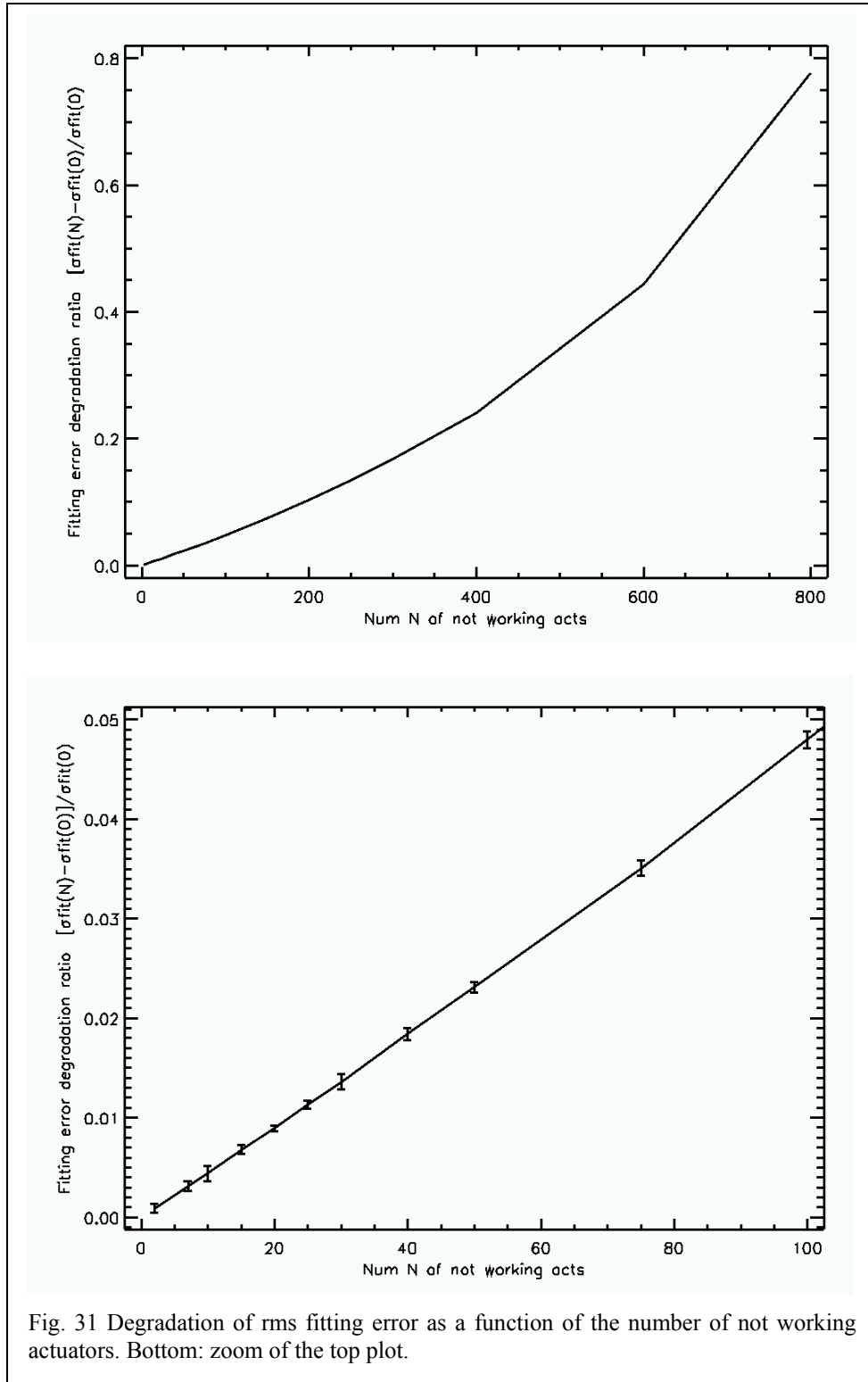Fig. 29 Mean seeing conditions. Maximum inter-actuator position stroke.

Fig. 30.Median seeing conditions. Maximum inter-actuator force stroke.

Fig. 31 Degradation of rms fitting error as a function of the number of not working actuators. Bottom: zoom of the top plot.

7   Actuator position structure function

Fig. 28 shows the actuator position structure functions when correcting median and bad seeing turbulence. The curves (black solid) match very well the theoretical structure function (red lines).

8   Position and force inter-actuator stroke

Fig. 29 and Fig. 30 show the map of maximum simulated inter-actuator position and force stroke for each actuator in median seeing conditions. Inter-actuator distance ranges between 28 and 41 mm.

9   Degradation of correction in case of not working actuators

DSM is weakly sensitive to actuator failure because actuators are non-contact voice-coil motor. In case some actuator is not working, internal control can be switched off and neighboring actuators can easily manage the new configuration. No stacked dips or bumps as in case of damaged piezo-stack actuators. The effect of increasing the number of disabled actuators turns in a smooth increase of fitting residual error due to the reduction of the number of degree of freedom as shown in Fig. 31. The fitting error degrades less then 5% when up to 100 actuators are out of order. The reduction of performances in terms of dynamics is still under investigation.

10   Numerical simulation results: correction as a function of number of mirror modes

The full correction analysis shows that the current actuator geometry of VLT-DSM is able to perform fitting errors below the threshold stated by the specification document. A modal correction analysis allows to define the minimum number of mirror modes to correct in order to meet the specifications. Reducing the number of modes helps to reduce the rms and peak force (i.e. power dissipation) especially in bad seeing conditions. Moreover the modal analysis is also important to define the DSM performances when the number of correcting modes of the DSM has to be reduced and optimized, for instance in case of faint guide stars.

10.1   Median seeing case

Fig. 32 and Fig. 33 show the rms wave-front residue and rms force as a function of the number of correcting mirror modes. The specified fitting error threshold is met using 633 of the 1170 modes. The first plot reports the Karhuenen-Loève fitting error, showing the good matching with mirror modes beyond the first ~50 modes. Results are summarized in the following table.

Parameter	Value
Median seeing@30deg: $r_0(0.5\mu m)$	12.1 cm
Specified fitting error	78 nm rms
No. of mirror modes to obtain spec	633
rms force to obtain spec	0.064 N rms

10.2 Bad seeing case

Similar plots for the bad-seeing case are shown in Fig. 34 and Fig. 35. In this case the specified threshold of fitting error is met using the first 738 mirror modes. The reduction of modes is important in this case in order to reduce rms force requirements to values below 0.20 N (see table below).

Parameter	Value
Bad seeing: $r_0(0.5\mu m)$	5.2 cm
Specified fitting error	149 nm rms
No. of mirror modes to obtain spec	738
rms force to obtain spec	0.165 N rms

Actuator distributions of peak and rms force are shown in Fig. 36 and Fig. 37. Fig. 38 shows the rms map of wave-front residuals. Table 8 summarizes the results. Required peak force is below 1 N threshold.

10.3 Direct comparison among mirror, Zernike and KL correction

Fig. 39 shows the ratio between modal mirror (solid black) or Zernike (red) residual fitting error with respect to the corresponding Karhunen-Loève residual fitting error as a function of the number of corrected modes. Mirror modes are as efficient as KL modes in correcting turbulence. The matching in performances (residual rms) is better then 4% when more then modes 50 modes are corrected.

11 Temporal behavior of turbulence correction

Temporal series of actuator position and force commands have been simulated generating larger phase screen (64m x 64m) and using the Taylor (frozen-turbulence) hypothesis. The wind speed is set to 18 m/s. The power spectral density of actuator position and force commands are shown in Fig. 40 and Fig. 41. In order to reduce computation time during the phase screen generation, in ths case the outer scale has been set to 150 m.
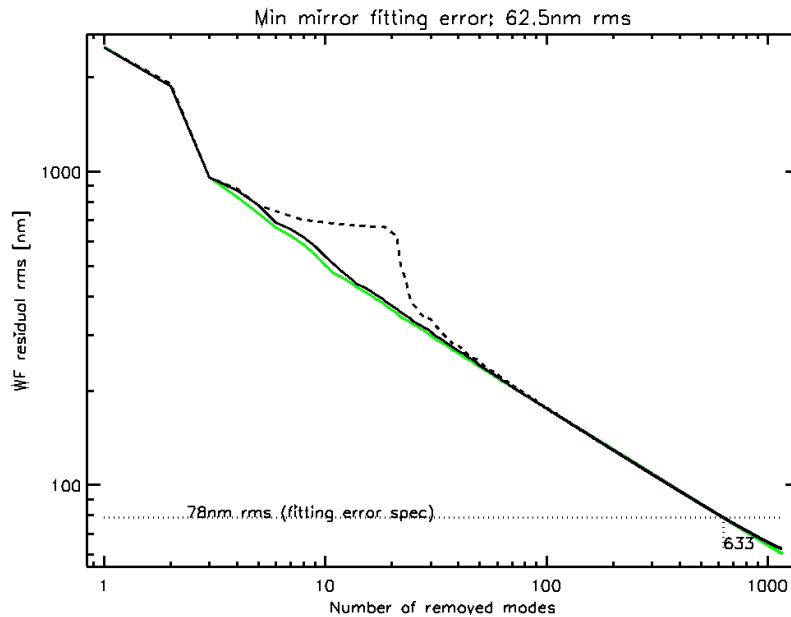
Fig. 32. Median seeing case. Fitting error as a function of the number of removed modes. Black solid mirror modes ordered with decreasing turbulence power content (optimized for fitting error). Black dashed: mirror modes ordered with increasing stiffness (optimized for power dissipation). Green: Karhunen-Loève modes. The specified fitting error (78 nm rms) is obtained removing 633 mirror modes.
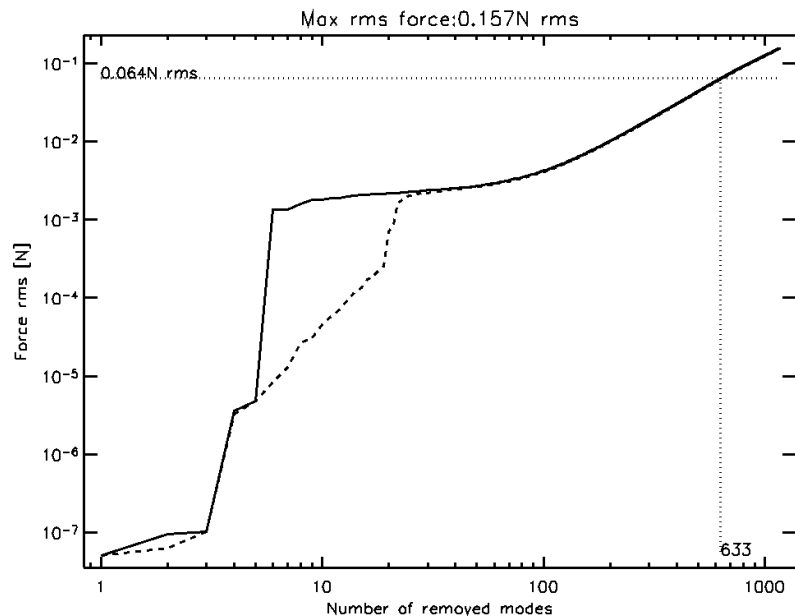

Fig. 33. Median seeing case. Rms force as a function of the number of removed modes. Black solid mirror modes ordered with decreasing turbulence power content (optimized for fitting error). Black dashed: mirror modes ordered with increasing stiffness (optimized for power dissipation).
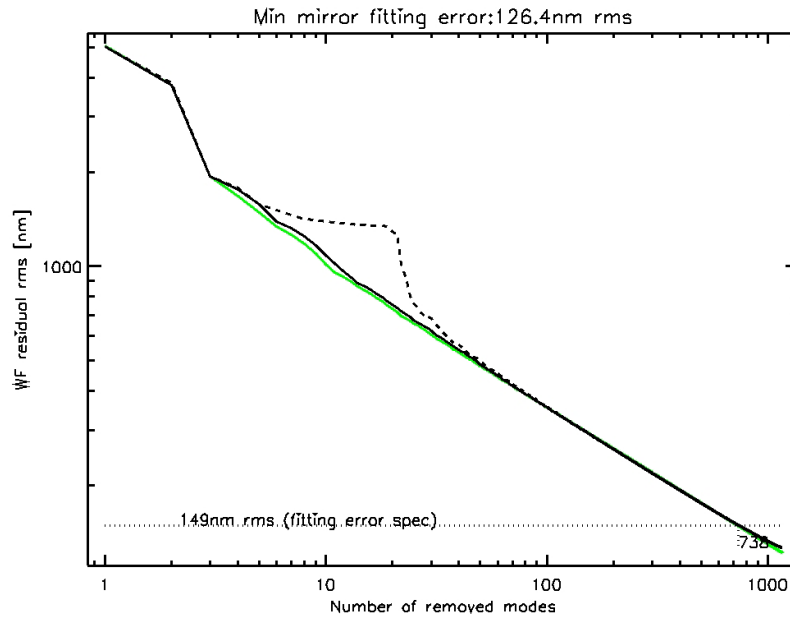
Fig. 34. Bad seeing case. Fitting error as a function of the number of removed modes. Black solid mirror modes ordered with decreasing turbulence power content (optimized for fitting error). Black dashed: mirror modes ordered with increasing stiffness (optimized for power dissipation). Green: Karhunen-Loève modes. The specified fitting error (149 nm rms) is obtained removing 738 mirror modes.
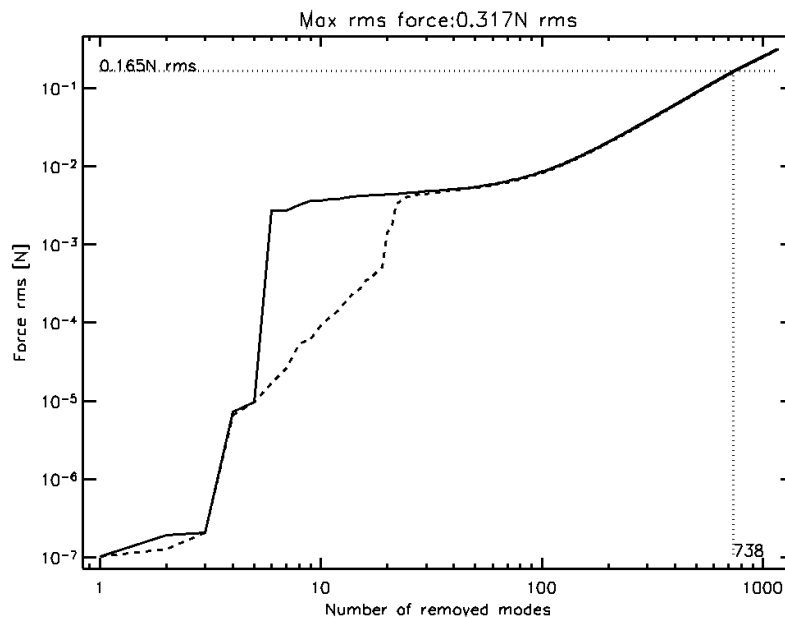

Fig. 35. Bad seeing case. Rms force as a function of the number of removed modes. Black solid mirror modes ordered with decreasing turbulence power content (optimized for fitting error). Black dashed: mirror modes ordered with increasing stiffness (optimized for power dissipation).
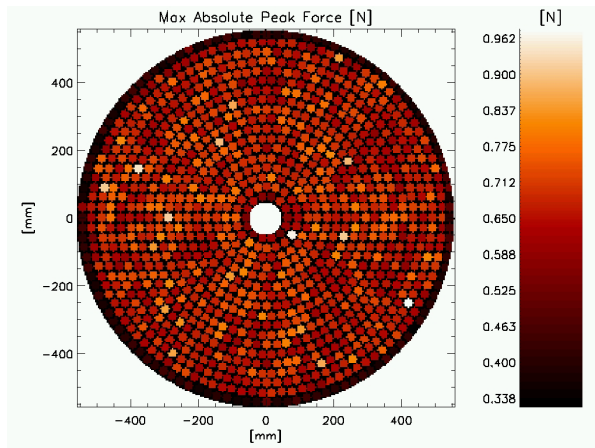
Fig. 36. Peak actuator force in bad seeing conditions removing 738 mirror modes. Result of fitting 10000 uncorrelated wave-fronts.
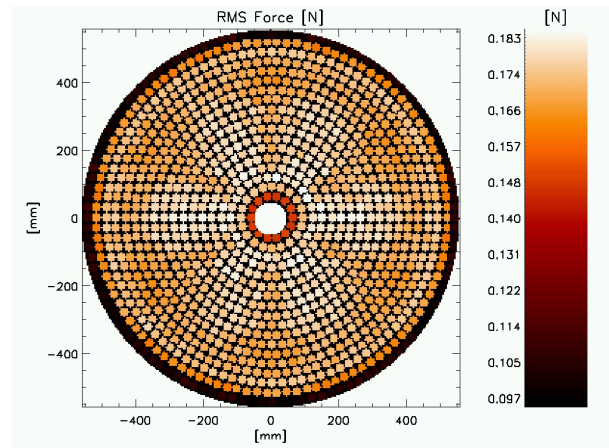

Fig. 37 Rms actuator force in bad seeing conditions removing 738 mirror modes. Result of fitting 10000 uncorrelated wave-fronts.
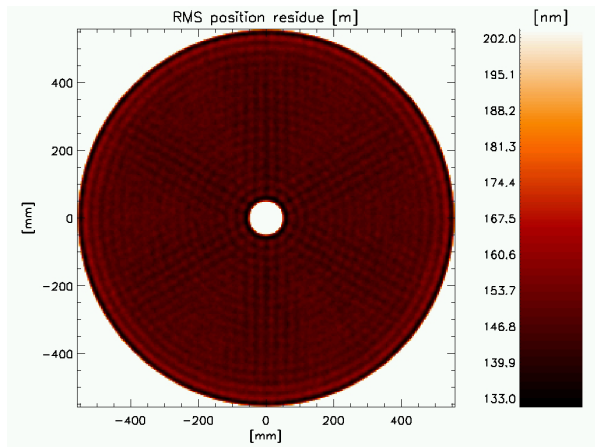

Fig. 38 Pupil map of the rms WF residual in bad seeing conditions removing 738 mirror modes. Result of fitting 10000 uncorrelated wave-fronts.

Parameter	Value
Bad seeing: $r_0(0.5\mu m)$	5.2 cm
Specified fitting error	149 nm rms
Fitting error (738 modes)	149 nm rms
max peak force (738 modes)	0.96 N
max rms actuator force (738 modes)	0.18 N rms
rms force (738 modes)	0.165 N rms

Table 8. Resume of the simulation results in the bad seeing case removing 738 mirror modes. Results of fitting 10000 uncorrelated wave-fronts.
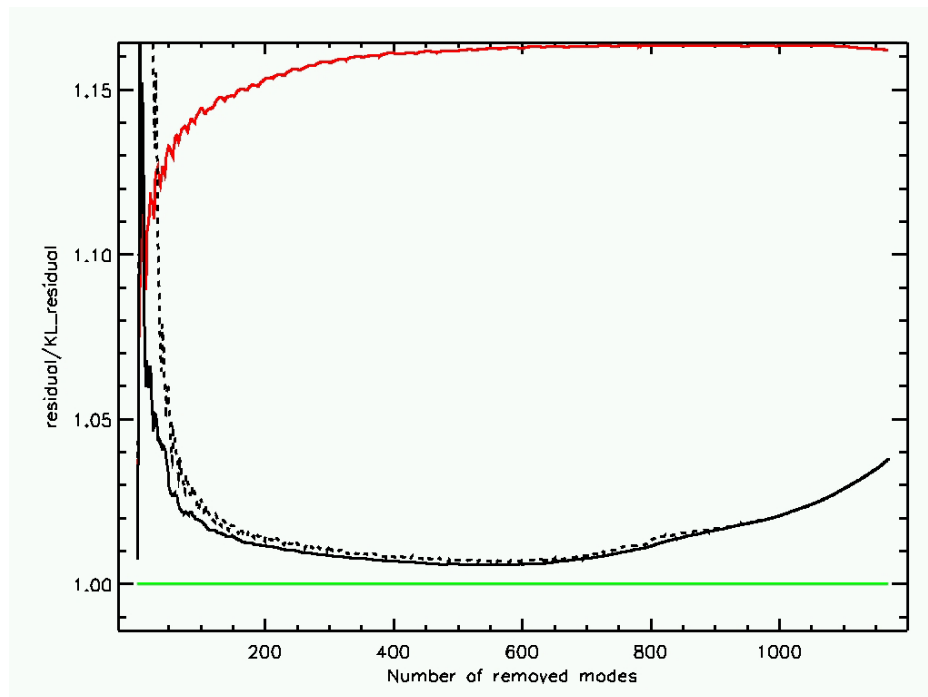
Fig. 39 Ratio between modal mirror (solid black) or Zernike (red) residual fitting error with respect to the corresponding Karhunen-Loève residual fitting error as a function of the number of corrected modes. Mirror modes are as efficient as KL modes in correcting turbulence. The matching in performances (residual rms) is better then 4% when more then modes 50 modes are corrected.

Fig. 40 PSD of actuator positions (black) and turbulence (red). 1 ms sampling, 18 m/s wind speed. Vertical dotted line corresponds to temporal frequency associated to Nyquist spatial sampling of actuator ((wind speed)/(2 times the pitch) = 42 Hz)
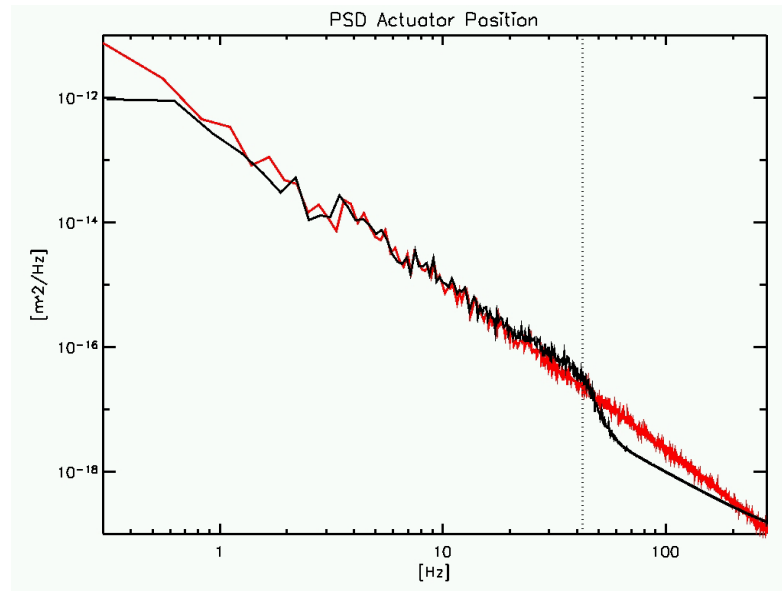

Fig. 41 PSD of actuator force. 1 ms sampling, 18 m/s wind speed. Vertical dotted line corresponds to temporal frequency associated to Nyquist spatial sampling of actuator ((wind speed)/(2 times the pitch) = 42 Hz).

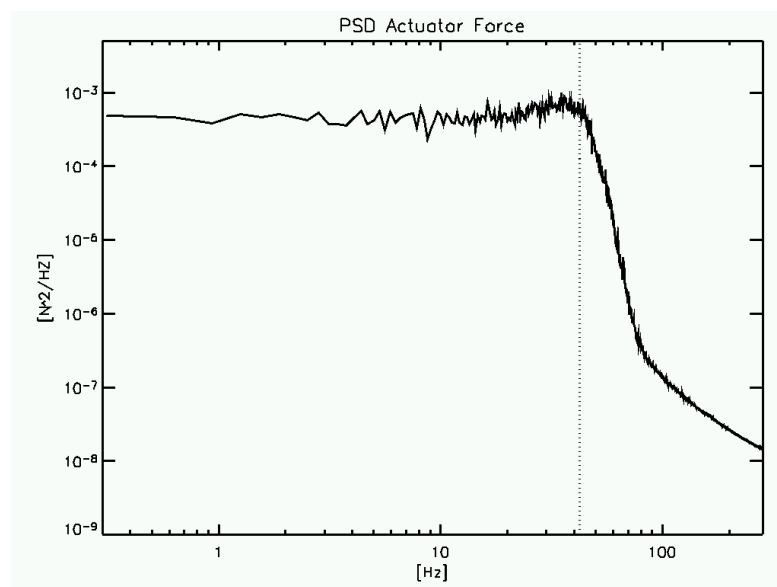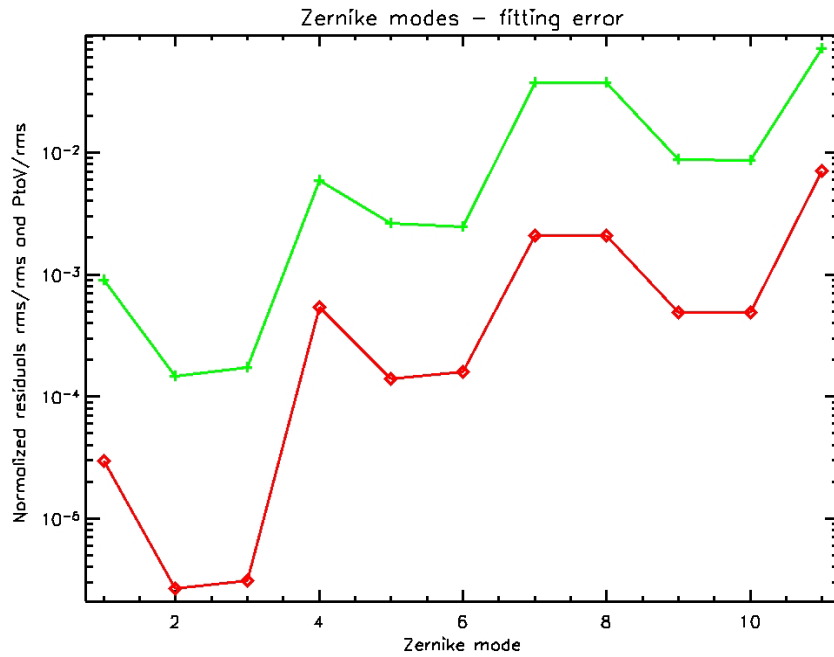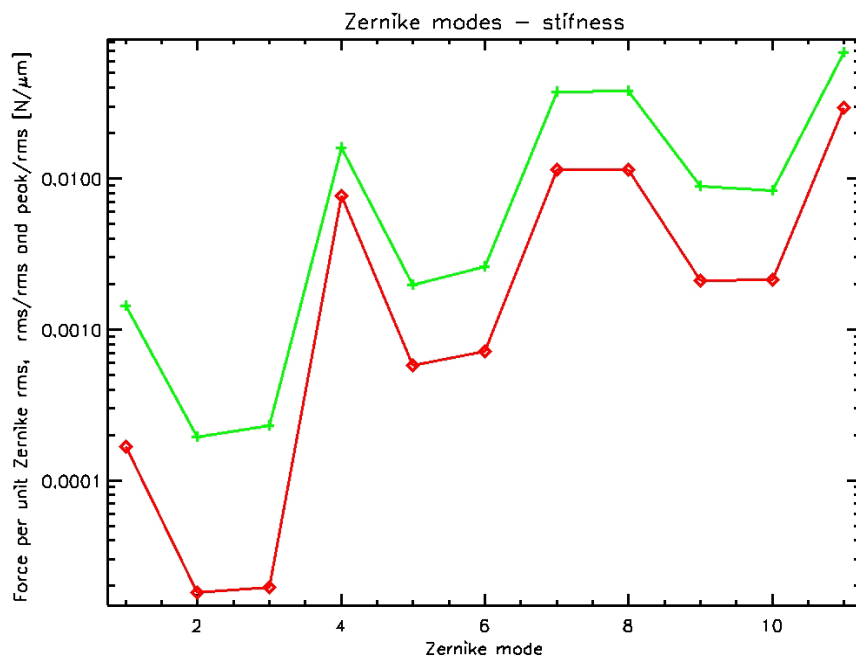Fig. 42 ratio between the fitting residual rms (red line) or PtV (green line) of the j-th Zernike P_j and the rms of $.P_j$

Fig. 43 ratio between the force rms (red line) or peak force (green line) to fit the j-th Zernike polynomial and the rms of Pj

Zern index	1	2	3	4	5	6	7	8	9	10	11
name	piston	tip	tilt	focus	astig	astig	coma	coma	trefoil	trefoil	spherical
Max applicable rms [µm]	70	520	430	6.3	51	39	2.7	2.6	11	12	1.5

Table 9. Maximum allowed Zernike rms that is applicable by the adaptive secondary shell. The maximum Zernike amplitude is limited by force constrains.

12 Fitting of Zernike deformations to compensate optical collimation error

In order to compensate telescope tracking errors and collimation errors between primary and secondary, it is interesting to analyze how well the adaptive secondary can apply the first 11 Zernike modes (from piston to spherical aberration). Fig. 42 shows the ratio between the fitting residual rms (red line) or PtV (green line) of a given Zernike polynomial P_j and the rms of $.P_j$. Fig. 43 shows the ratio between the force rms (red line) or peak force (green line) to fit the j-th Zernike polynomial and the rms of P_j. The stiffness and fitting residuals of piston and tip-tilt terms are due to the effects induced by the central membrane (axial stiffness 9.2 N/mm).

The amplitude of a given Zernike polynomial has two limitations (See Ref. [9], Sec. 1):

1. peak force reaches a given threshold (for instance 1/10 of the max force f_{max} that an actuator can apply)

2. the residual error reaches a given fraction of the turbulence fitting error σ_{fit} in good seeing conditions (for instance 1/3 of σ_{fit}, i.e. 1/9 in variance)

Stating f_{max}=1 N and σ_{fit}=41 nm rms (fitting error scaled for r_0=0.20 m with λ=0.5µm), the max applicable rms values of the first 11 Zernike polynomials are reported in Table 9. The values are constrained by the second condition (force constrain).

13 Flattening of shell manufacturing errors

Using FEA influence functions it is possible to refine the flattening specifications stated in Ref. [9] taking in account the correct actuator geometry, shell curvature and edge effects. Previous work considered a simplified model to obtain an analytical solution.

The natural modal basis for describing the manufacturing error would be the mirror modal base. However opticians usually require a description in term of better-known Zernike polynomials, so let us decompose the surface manufacturing error $s(x,y)$ in terms of Zernike polynomials

$$s(x,y) = \phi_{LO}(x,y) + \phi_{HO}(x,y), \quad \phi_{LO}(x,y) = \sum_{j}^{j\max} a_j^{LO} Z_j(x,y), \quad \phi_{HO}(x,y) = \sum_{j\max+1}^{\infty} a_j^{HO} Z_j(x,y),$$

where $\phi_{LO}(x,y)$ ($j \leq j_{max}$) and $\phi_{HO}(x,y)$ ($j > j_{max}$) are, respectively, the low and high order components of the surface error. Stating $j_{max} = 1176$ and following Ref. [9] (Sec. 6 and 7) numerical data we can specify that:
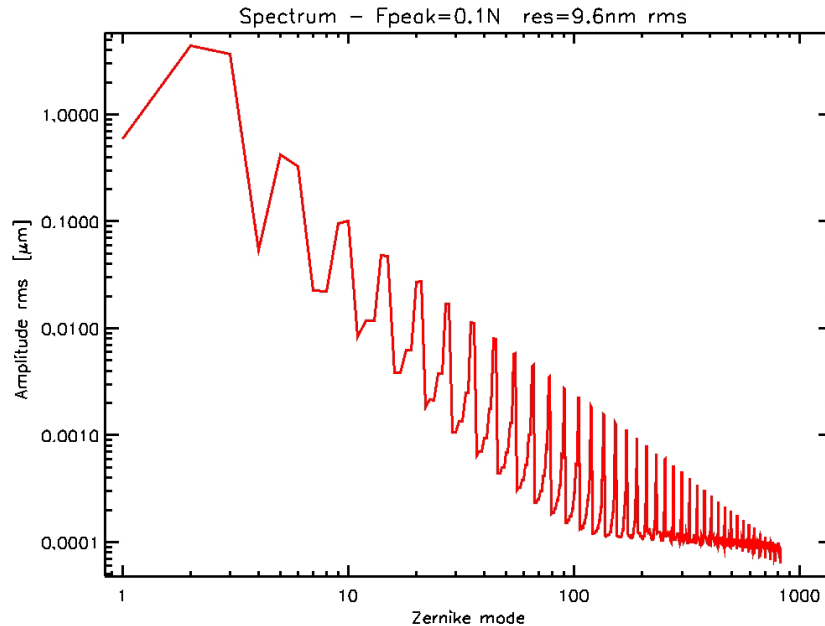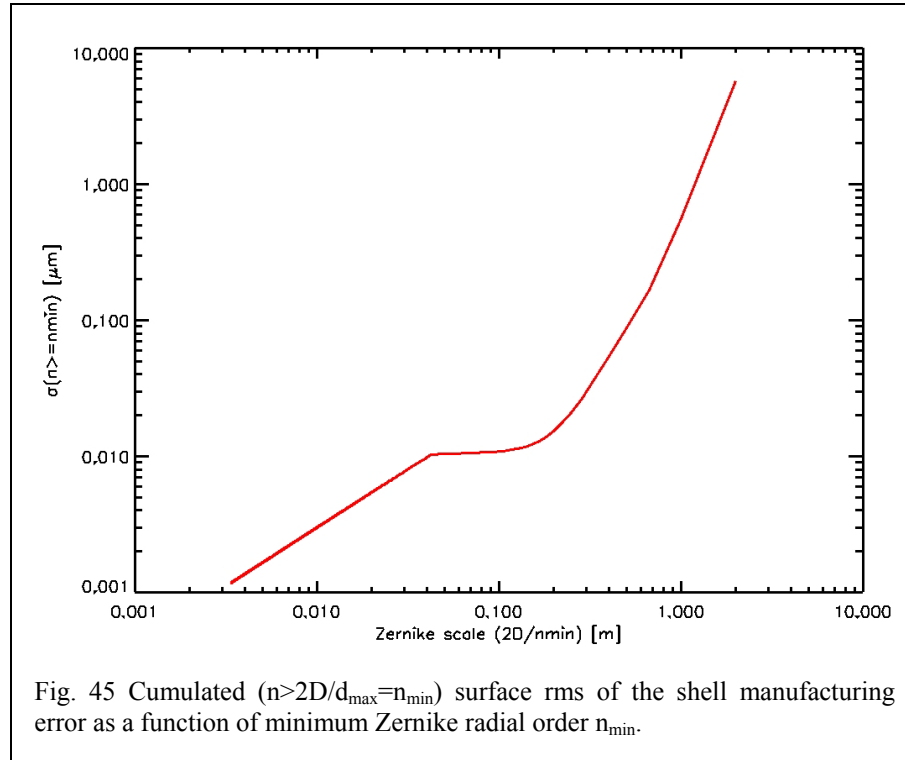
Fig. 44 Allowed envelope of Zernike coefficient spectrum for the shell surface manufacturing error. The limitation on the coefficient amplitudes is dominated by peak force threshold (0.1 N).

- surface rms of high order component $\phi_{HO}(x,y)$ (essentially not corrected by the mirror) has to be less than 9.6 nm rms, corresponding to the AO fitting residual in case of extremely good seeing (0.21 arcsec, r_0=0.5 m at λ=0.5 µm);

- the component $\phi_{LO}(x,y)$ is highly compensated by the actuators. The surface rms of the residual of this correction has to be, again, less than 9.6 nm rms;

- at the same time, the peak force to compensate $\phi_{LO}(x,y)$ has to be less than 0.1 N, i.e. 1/10 of the force actuator stroke.

The last two conditions give the envelope of the absolute value for the Zernike coefficients a_j^{LO} (j=1, 2, …,j_{max}=1176) that is shown in Fig. 44. Of course first three modes (piston, tip and tilt) can be corrected by a suitable alignment of the whole DSM unit using the hexapod and can be not considered. The high oscillations in the coefficient spectrum correspond to the various radial orders. For each radial order there is a lowest peak corresponding to axial-symmetrical (stiff, low azimuthal order) modes and a highest peak corresponding to the n-foil (floppy, high azimuthal order) mode.

Defining a characteristic Zernike scale as d=2D/n, where n is the Zernike radial order, we can compute the cumulative surface rms of the manufacturing error with spatial scales d smaller than d_{max}, i.e. for Zernike components having radial degree n larger then n_{min}=2D/d_{max}. The result is reported in Fig. 45, which is the corresponding graph of Fig. 2 in Ref. [9], but here obtained using FEA data instead of a simplified analytical model.

Fig. 45 Cumulated ($n > 2D/d_{max} = n_{min}$) surface rms of the shell manufacturing error as a function of minimum Zernike radial order n_{min}.

14 Conclusions

The proposed geometry of actuators (1170) is able to perform the specified fitting error both in median and bad seeing conditions. Considering the shell thickness of 2.0 mm, in bad seeing conditions the number of correcting modes has to be limited to 738 of the available 1170 in order to keep the peak force within 1 N and the rms force below 0.2 N. The simulation provided force patterns to Microgate Srl to dimension current driver electronics and to ADS Internationsl Srl to dimension the cooling lines.

References

[1] D. Gallieni, "*VLT DSM feasibility study. Opto-mechanical design,*" VLT-TRE-ADS-11250-3634, Issue 1, 04 May 2005.

[2] R. Arsenault and N. Hubin, "*Technical specifications for the design study of an Adaptive Secondary Mirror for the VLT,*" VLT-SPE-ESO-11250-3068, Issue 2, 10 May 2004.

[3] P. Dierickx, "*VLT Optics: design of telescope optics,*" VLT-TRE-ESO-10000-526, Issue 1.B, 24 Feb 1995.

[4] M. Carbillet, C. Vérinaud, B. Femenía, A. Riccardi, and L. Fini, "*Modelling astronomical adaptive optics - I. The software package CAOS,*" *MNRAS*, **356**, pp. 1263-1275, Feb. 2005.

[5] R.C. Cannon, "*Optimal bases for wave-front simulation and reconstruction on annular apertures,*" J. Opt. Soc. Am. A, **13**, pp. 862-867, 1996.

[6] G. Dai, "*Modal wavefront reconstruction with Zernike polynomials and Karhunen-Loève function*," J. Opt. Soc. Am. A, **13**, pp. 1218-1225, 1996.

[7] D. M. Winker, "*Effect of a finite outer scale on the Zernike decomposition of atmospheric optical turbulence*," J. Opt. Soc. Am. A, **8**, pp. 1568-1573, 1991

[8] N. Takato, I. Yamaguchi, "*Spatial correlation of Zernike phase-expansion coefficients for atmospheric turbulence with finite outer scale*," J. Opt. Soc. Am. A, **12**, pp. 958-963, 1995.

[9] A. Riccardi, "*Optical figuring specifications for thin shells to be used in adaptive telescope mirror*," VLT-SPE-OAA-11255-0001, Issue 1, 21 Oct 2004.
(http://www.arcetri.astro.it/pubblicazioni/Reports/04/4_04.html)